https://doi.org/10.5194/egusphere-2024-2395
Preprint. Discussion started: 31 January 2025

Modeling L-band Microwave Brightness Temperature Time Series for Firn Aquifers

Haokui Xu[1], Leung Tsang[1], Julie Miller[2], Brooke C. Medley[3,] Joel T. Johnson[4]

[1]Department of Electrical Engineering and Computer Sciences, University of Michigan, Ann Arbor, MI, 48105, U.S.A
[2] Earth Science and Observation Center, Cooperative Institute for Research in Environmental Sciences, University of Colorado Boulder, Boulder, CO 80309 USA
[3]Earth Science Divisions, NASA Goddard Space Flight Center, ,Green Belt, MD, 20771, U.S.A
[4]ElectroScience Lab, The Ohio State University, Columbus, OH, 43210, U.S.A

Correspondence to: Haokui Xu (xuhaoku@umich.edu)

Abstract. Firn aquifers are important in polar ice sheet hydrology and the associated mass and energy transport processes. Although the firn aquifer extent has been mapped using passive microwave satellite observations, models for predicting the L-band brightness temperature time series have remained elusive. This paper implements a radiative transfer model for time series L-Band V and H pol brightness temperature (TB) observations from the 3 km SMAP enhanced resolution data product. The model relates the firn aquifer permittivity and properties of the dry firn layer above the aquifer to SMAP observations. Results are presented for aquifers within both the Greenland and Antarctic ice sheets. The results show that the brightness temperature is more sensitive to aquifer liquid water content changes when the water table is closer to the surface. The method provides a tool for the radiometry study of firn aquifer and a theoretical basis for potentially retrieving firn aquifer liquid water content using passive microwave data.

1 Introduction

Summer surface melt in the percolation facets of the Greenland Ice Sheet (GrIs) and the Antarctic Ice Sheet(AIS) is an important process [Mankoff et al. 2021, Lenaerts et al. 2019]. An extreme event in 2012, for example, produced surface melt over the entire GrIS [Nghiem et al. 2012]. Meltwater is typically expected to refreeze locally within the firn or run off into the ocean. However, under certain conditions, an ice-water mixed layer called the Perennial firn aquifer can remain unfrozen during the winter season. A major discovery of an aquifer occurred in 2011 on the southeastern coast of Greenland during the Arctic Circle Traverse expedition, which involved a drilled borehole and GPR survey [Foster et al. 2013]. If drained, Greenland aquifers could contribute up to a 0.4 mm increase in sea level [Koenig et al. 2014].

Instead of simply acting as a meltwater store, the embedded water can flow and drain the aquifer quickly [Miller et al. 2018], and studies have shown an average aquifer age of 6.5 years [Miller et al. 2020]. This indicates that the aquifer is not buffering the mass loss or the rise of the sea level but perhaps delaying its contribution. Understanding the aquifer's water content can help close the mass balance of Greenland and the meltwater routing mechanism.

https://doi.org/10.5194/egusphere-2024-2395
Preprint. Discussion started: 31 January 2025

Firn aquifers have been mapped using airborne GPR data from Operation Ice Bridge [Miège et al. 2016, Chu et al. 2018]. The total amount of water was estimated in regions where the ice-ground reflection could be observed, from which the decay due to the aquifer layer could be estimated [Chu et al. 2018]. Such studies are limited to the available flight paths, and GPR data were gathered only once yearly in the late spring. Mapping for the horizontal extent of the firn aquifer from satellite data was first performed using Sentinel-1 C band SAR data [Brangers et al. 2020].

L-band brightness temperatures from the Soil Moisture Active and Passive (SMAP) [Entekhabi et al. 2010, Long et al. 2019] mission satellite have also been used in firn aquifer studies. Brightness temperature data shows a logistic-like decrease in brightness temperature from late summer to late spring of the next year due to increased scattering from dry firn [Miller et al. 2020]. The horizontal extent of the Greenland aquifers was then mapped based on time series signatures in enhanced resolution SMAP brightness temperature data. A saturation factor was also derived from time series data to first map the percolation zone and then identify the aquifer and subsurface ice slab [Miller et al., 2022]. However, the liquid water content inside the aquifer has not been quantitatively studied. Due to the low absorption of ice and air, thermal emission from a firn aquifer is modulated by the aquifer-firn interface and the dry firn structure above. Though modeling efforts have been made to explain the time series of the brightness temperature, a simple layered random medium model is not capable of explaining the polarization dependence in the measurements [Bringer et al. 2017].

In this paper, a radiative transfer model based on 3-dimensional firn profiles [Tsang et al. 2001, Xu et al. 2023] and an effective permittivity of the aquifer [Huang et al. 2024], predicted from a full wave approach is used to explain brightness temperature time series and their polarization dependence. In modeling aquifer thermal emissions, two components need to be characterized. The first is a permittivity model for the firn aquifer, which is the key parameter that relates the firn-aquifer interface reflection to the water content of the aquifer. The second is a radiative transfer model that accounts for the reflection of thermal emission due to the firn-aquifer interface and for density variations in the dry firn. In the emission problem, the firn-aquifer interface produces upward emissions and also reflects downward emissions from the dry firn above. Multiple scattering also occurs within the dry firn layer due to its inhomogeneity. The approach also allows the possibility of estimating the water content of the aquifer remotely.

The analysis considers 3 km enhanced resolution SMAP brightness temperature time series data for two locations in Greenland and one in Antarctica. For Greenland, the 3 km pixels covering FA-13 (66.1812,-39.0435) [Koenig et al. 2014] and the "location 2" (66.19, -39.1685) about 5km from FA-13 are studied. FA-13 provides in situ measurements of density (Sumup data set [Montgomery et al. 2018]), temperature [Clément et al., 2020], and water level depth (position of aquifer upper boundary); density and temperature profiles are assumed identical at location 2. The two locations lie on a 2014 survey path of the University of Kansas Accumulation Radar [CReSIS 2024]. The water table depth at location 2 is obtained from the Accumulation Radar echogram. The final location lies on the Wilkins Ice Shelf [Montgomery et al., 2020], Antarctica, where a field investigation was performed in Dec 2018. The investigation provides information on the density profile and the water table depth. Temperature and liquid water content information are not available in this location; other in situ information on the Wilkins Ice Shelf is available on the website of the U.S. Antarctic Program (USAP) Data Center [Miège 2020].

https://doi.org/10.5194/egusphere-2024-2395
Preprint. Discussion started: 31 January 2025

Information from the in-situ measurements is applied with the forward model to simulate SMAP V and H-pol brightness temperatures. Data collected from winter 2015 to summer 2016 in Greenland and during 2018 for the Wilkins Ice Shelf is analyzed.

The next section illustrates the physical model for the thermal emission problem. First, mathematical derivations for the radiative transfer model are described, and a discussion of aquifer permittivity is then provided. In Section 3, the data sets used are discussed. The numerical results are presented together with the SMAP measurements over Greenland's east coast from winter 2015 to Spring 2016 and over Wilkins Ice Shelf in 2018. Additional discussions and conclusions are then provided in Sections 4 and 5, respectively.

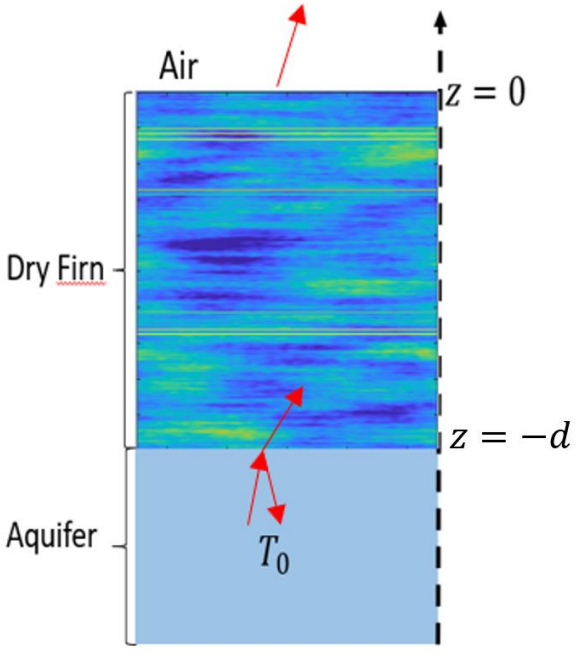

Figure 1 A two-layer model for the firn aquifer region in the early spring before surface melting starts. Three-dimensional varying profiles characterize the firn region. Deep blues means relatively lower density, while yellow means relatively higher density. The aquifer is characterized as a mixture of ice and water. Due to the permittivity contrast of dry firn and aquifer, the interface is a reflective boundary.

2 Method

The model describes a firn aquifer as the two-region structure illustrated in Figure 1: dry firn on top of a saturated aquifer. The thickness of the dry firn layer is denoted as d , where $z = -d$ is the water level depth (upper aquifer boundary). The dry firn is described as a random medium having permittivity fluctuations (due to ice density variations) in both the vertical and horizontal directions, as well as a mean value that varies with depth. The mean density profile is obtained by fitting the borehole density measurements with an exponential curve. The fluctuating profile is characterized by the following correlation function:

https://doi.org/10.5194/egusphere-2024-2395
Preprint. Discussion started: 31 January 2025

$$C(\vec{r},\vec{r}') = \Delta^2 \exp\left(-\frac{|z-z'|}{l_z}\right)\exp\left(-\frac{|\vec{r}_\perp - \vec{r}'_\perp|^2}{l_\rho^2}\right)$$

Where $\Delta = std(\rho)$ is the standard deviation of the density fluctuations, with l_z and l_ρ , the vertical and horizontal correlation lengths. Density fluctuations in the vertical direction are modeled as exponentially correlated, while those in the horizontal direction are modeled with a Gaussian function. This model of 3D variations was previously used to model brightness temperatures over the accumulation zone in Greenland [Xu 2024]; the 3-dimensional variations represented cause angular and polarization coupling between V and H polarizations that was found to improve the match to measured data. Previously, the lower boundary of the variation region was considered to have no reflection. In this case, due to the existence of a firn aquifer, the reflection from this boundary could not be ignored.

Because aquifers usually exist in the percolation zone of the ice sheet, their density properties can be very different from those in the accumulation zone, where the freeze-thaw process is rare. Borehole measurements indicate a high-density variation profile in the firn above an aquifer.

2.1 Radiative transfer model in the dry zone region

The emission can be described in the dry zone region by the coupled radiative transfer equations:

$$cos\theta \frac{d}{dz}\vec{T}_u(\theta,z) = -\overleftrightarrow{\kappa_e}(\theta,z)\vec{T}_u(\theta,z) + \kappa_a(z)T_0(z) + \int_0^{\frac{\pi}{2}} d\theta' sin\theta' \left[\overleftrightarrow{P}(\theta,\theta',z)\vec{T}_u(\theta',z) + \overleftrightarrow{P}(\theta,\pi-\theta',z)\vec{T}_d(\theta',z)\right]$$

$$-cos\theta \frac{d}{dz}\vec{T}_d(\theta,z) = -\overleftrightarrow{\kappa_e}(\theta,z)\vec{T}_d(\theta,z) + \kappa_a(z)T_0(z) + \int_0^{\frac{\pi}{2}} d\theta' sin\theta \left[\overleftrightarrow{P}(\pi-\theta,\theta',z)\vec{T}_u(\theta',z) + \overleftrightarrow{P}(\pi-\theta,\pi-\theta',z)\vec{T}_d(\theta',z)\right]$$

Where $\vec{T}_u(\theta,z)$ and $\vec{T}_d(\theta,z)$ are the upward and downward brightness temperatures, $\overleftrightarrow{\kappa_e}(\theta,z)$ is the extinction coefficient matrix, $\kappa_a(z)$ is the absorption coefficient. $\overleftrightarrow{P}(\theta,\theta',z)$ is the phase matrix that couples the brightness temperature in θ' to the direction of θ. The parameters in the radiative transfer equations are functions of depth. This is because the temperature and density profiles vary according to the depth. The radiative transfer equations are subject to the boundary conditions:

$$\vec{T}_d(\theta,z=0) = \overleftrightarrow{R_{10}}(\theta)\vec{T}_u(\theta,z=0)$$

$$\vec{T}_u(\theta,z=-d) = \overleftrightarrow{R_{12}}(\theta)\vec{T}_d(\theta,z=-d) + \left(1-\overleftrightarrow{R_{12}}(\theta)\right)T_{aquifer}$$

where $\overleftrightarrow{R_{10}}(\theta)$ and $\overleftrightarrow{R_{12}}(\theta)$ are diagonal reflectivity matrices for the dry firn-air interface (the upper boundary of the dry firn region) and the dry firn-aquifer interface (the low boundary of the dry firn region). At the dry firn-aquifer interface, the brightness temperature emitted from the aquifer is transmitted into the dry firn region, as indicated by the term $\left(1-\overleftrightarrow{R_{12}}(\theta)\right)T_{aquifer}$ where $T_{aquifer}$ is the aquifer's physical temperature.

https://doi.org/10.5194/egusphere-2024-2395
Preprint. Discussion started: 31 January 2025

The radiative transfer equations are solved using an iterative approach. The differential equations are converted into integral equations that express the upward and downward brightness temperature in terms of integrals. Details on how to obtain the expressions are documented in [Xu 2024], and major steps are listed in the Appendix.

The final expressions for the upward and downward brightness temperatures are:

$$\overrightarrow{T_u}(\theta,z) = \left[I - \vec{r}_{10}(\theta)\vec{r}_{12}(\theta)\exp\left(-2\sec\theta\int_{-d}^{0}\overrightarrow{\kappa_e}(\theta,z'')dz''\right)\right]^{-1}\exp\left(-\sec\theta\int_{-d}^{z}\overrightarrow{\kappa_e}(\theta,z'')dz''\right)(1-\vec{r}_{12}(\theta))T_2$$

$$+\sec\theta\int_{-d}^{z}\kappa_a(z')T_0(z')\exp\left(-\sec\theta\int_{z'}^{z}\overrightarrow{\kappa_e}(\theta,z'')dz''\right)dz'$$

$$+\left[I - \vec{r}_{10}(\theta)\vec{r}_{12}(\theta)\exp\left(-2\sec\theta\int_{-d}^{0}\overrightarrow{\kappa_e}(\theta,z'')dz''\right)\right]^{-1}\exp\left(-\sec\theta\int_{-d}^{z}\overrightarrow{\kappa_e}(\theta,z'')dz''\right)\vec{r}_{12}(\theta)\sec\theta$$

$$\int_{-d}^{0}\kappa_a(z')T_0(z')\exp\left(-\sec\theta\int_{-d}^{z'}\overrightarrow{\kappa_e}(\theta,z'')dz''\right)dz'$$

$$+\left[I - \vec{r}_{10}(\theta)\vec{r}_{12}(\theta)\exp\left(-2\sec\theta\int_{-d}^{0}\overrightarrow{\kappa_e}(\theta,z'')dz''\right)\right]^{-1}\exp\left(-\sec\theta\int_{-d}^{z}\overrightarrow{\kappa_e}(\theta,z'')dz''\right)\vec{r}_{10}(\theta)\vec{r}_{12}(\theta)\sec\theta$$

$$\exp\left(-\sec\theta\int_{-d}^{0}\overrightarrow{\kappa_e}(\theta,z'')dz''\right)\int_{-d}^{0}\kappa_a(z')T_0(z')\exp\left(-\sec\theta\int_{z'}^{0}\overrightarrow{\kappa_e}(\theta,z'')dz''\right)dz'$$

$$+\vec{S}(\theta,z)$$

$$+\left[I - \vec{r}_{10}((\theta)\vec{r}_{12}(\theta)\exp\left(-2\sec\theta\int_{-d}^{0}\overrightarrow{\kappa_e}(\theta,z'')dz''\right)\right]^{-1}\vec{r}_{12}(\theta)\overrightarrow{W}(\theta,-d)\exp\left(-\sec\theta\int_{-d}^{z}\overrightarrow{\kappa_e}(\theta,z'')dz''\right)$$

$$+\left[I - \vec{r}_{10}(\theta)\vec{r}_{12}(\theta)\exp\left(-2\sec\theta\int_{-d}^{0}\overrightarrow{\kappa_e}(\theta,z'')dz''\right)\right]^{-1}$$

$$\vec{r}_{10}(\theta)\vec{r}_{12}(\theta)\exp\left(-\sec\theta\int_{-d}^{z}\overrightarrow{\kappa_e}(\theta,z'')dz''\right)\exp\left(-\sec\theta\int_{-d}^{0}\overrightarrow{\kappa_e}(\theta,z'')dz''\right)\vec{S}(\theta,0)$$

For the downward component:

$$\overrightarrow{T_d}(\theta,z) = \left[I - \vec{r}_{12}(\theta)\vec{r}_{10}(\theta)\exp\left(-2\sec\theta\int_{-d}^{0}\overrightarrow{\kappa_e}(\theta,z'')dz''\right)\right]^{-1}\exp\left(-\sec\theta\int_{z}^{0}\overrightarrow{\kappa_e}(\theta,z'')dz''\right)\vec{r}_{10}(\theta)$$

$$(1-\vec{r}_{12}(\theta))T_2\exp\left(-\sec\theta\int_{-d}^{0}\overrightarrow{\kappa_e}(\theta,z'')dz''\right)$$

$$+\sec\theta\int_{z}^{0}\kappa_a(z')T_0(z')\exp\left(-\sec\theta\int_{z}^{z'}\overrightarrow{\kappa_e}(\theta,z'')dz''\right)dz'$$

$$+\left[I - \vec{r}_{12}(\theta)\vec{r}_{10}(\theta)\exp\left(-2\sec\theta\int_{-d}^{0}\overrightarrow{\kappa_e}(\theta,z'')dz''\right)\right]^{-1}\exp\left(-\sec\theta\int_{z}^{0}\overrightarrow{\kappa_e}(\theta,z'')dz''\right)\vec{r}_{10}(\theta)$$

$$\sec\theta\int_{-d}^{0}\kappa_a(z')T_0(z')\exp\left(-\sec\theta\int_{z'}^{0}\overrightarrow{\kappa_e}(\theta,z'')dz''\right)dz'$$

https://doi.org/10.5194/egusphere-2024-2395
Preprint. Discussion started: 31 January 2025

$$+\left[I-\overrightarrow{r}_{12}(\theta)\overrightarrow{r}_{10}(\theta)\exp\left(-2\sec\theta\int_{-d}^{0}\overrightarrow{\kappa_e}(\theta,z'')dz''\right)\right]^{-1}\exp\left(-\sec\theta\int_{z}^{0}\overrightarrow{\kappa_e}(\theta,z'')dz''\right)\overrightarrow{r}_{12}(\theta)$$

$$\overrightarrow{r}_{10}(\theta)\exp\left(-\sec\theta\int_{-d}^{0}\overrightarrow{\kappa_e}(\theta,z'')dz''\right)\sec\theta\int_{-d}^{0}\kappa_a(z')T_0(z')\exp\left(-\sec\theta\int_{-d}^{z'}\overrightarrow{\kappa_e}(\theta,z'')dz''\right)dz'$$

$$+\overrightarrow{W}(\theta,z)$$

$$+\left[I-\overrightarrow{r}_{12}(\theta)\overrightarrow{r}_{10}(\theta)\exp\left(-2\sec\theta\int_{-d}^{0}\overrightarrow{\kappa_e}(\theta,z'')dz''\right)\right]^{-1}\exp\left(-\sec\theta\int_{z}^{0}\overrightarrow{\kappa_e}(\theta,z'')dz''\right)\overrightarrow{r}_{10}(\theta)\vec{S}(\theta,0)$$

$$+\left[I-\overrightarrow{r}_{12}(\theta)\overrightarrow{r}_{10}(\theta)\exp\left(-2\sec\theta\int_{-d}^{0}\overrightarrow{\kappa_e}(\theta,z'')dz''\right)\right]^{-1}\exp\left(-\sec\theta\int_{z}^{0}\overrightarrow{\kappa_e}(\theta,z'')dz''\right)\overrightarrow{r}_{12}(\theta)$$

$$\overrightarrow{r}_{10}(\theta)\exp\left(-\sec\theta\int_{-d}^{0}\overrightarrow{\kappa_e}(\theta,z'')dz''\right)\overrightarrow{W}(\theta,-d)$$

Each expression includes terms without scattering (the three terms at the beginning of each expression) and terms that involve scattering (the remaining four terms). The first and second terms are the direct contribution of the aquifer and dry firn emissions. The third term is the downwelling dry firn emission reflected from the aquifer interface. The fourth term is the scattering source term, while the fifth is scattering reflected at the boundary once. The last terms are scattering sources due to double reflections at upper and lower boundaries.

The terms without scattering are considered as the 0th-order solution in the iterative approach. The nth-order solutions are obtained by substituting the n-1 th-order term inside the scattering expressions as:

$$\overrightarrow{T_u}^{n}(\theta,z)=\vec{S}^{n}(\theta,z)$$

$$+\left[I-\overrightarrow{r}_{10}((\theta)\overrightarrow{r}_{12}(\theta)\exp\left(-2\sec\theta\int_{-d}^{0}\overrightarrow{\kappa_e}(\theta,z'')dz''\right)\right]^{-1}\overrightarrow{r}_{12}(\theta)\overrightarrow{W}^{n}(\theta,-d)\exp\left(-\sec\theta\int_{-d}^{z}\overrightarrow{\kappa_e}(\theta,z'')dz''\right)$$

$$+\left[I-\overrightarrow{r}_{10}(\theta)\overrightarrow{r}_{12}(\theta)\exp\left(-2\sec\theta\int_{-d}^{0}\overrightarrow{\kappa_e}(\theta,z'')dz''\right)\right]^{-1}$$

$$\overrightarrow{r}_{10}(\theta)\overrightarrow{r}_{12}(\theta)\exp\left(-\sec\theta\int_{-d}^{z}\overrightarrow{\kappa_e}(\theta,z'')dz''\right)\exp\left(-\sec\theta\int_{-d}^{0}\overrightarrow{\kappa_e}(\theta,z'')dz''\right)\vec{S}^{n}(\theta,0)$$

$$\overrightarrow{T_d}^{n}(\theta,z)=\overrightarrow{W}^{n}(\theta,z)$$

$$+\left[I-\overrightarrow{r}_{12}(\theta)\overrightarrow{r}_{10}(\theta)\exp\left(-2\sec\theta\int_{-d}^{0}\overrightarrow{\kappa_e}(\theta,z'')dz''\right)\right]^{-1}\exp\left(-\sec\theta\int_{z}^{0}\overrightarrow{\kappa_e}(\theta,z'')dz''\right)\overrightarrow{r}_{10}(\theta)\,\vec{S}^{n}(\theta,0)$$

$$+\left[I-\overrightarrow{r}_{12}(\theta)\overrightarrow{r}_{10}(\theta)\exp\left(-2\sec\theta\int_{-d}^{0}\overrightarrow{\kappa_e}(\theta,z'')dz''\right)\right]^{-1}\exp\left(-\sec\theta\int_{z}^{0}\overrightarrow{\kappa_e}(\theta,z'')dz''\right)\overrightarrow{r}_{12}(\theta)$$

https://doi.org/10.5194/egusphere-2024-2395
Preprint. Discussion started: 31 January 2025

$$\overleftrightarrow{r}_{10}(\theta)\exp\left(-\sec\theta\int_{-d}^{0}\overleftrightarrow{\kappa_e}(\theta,z'')dz''\right)\vec{W}^{n}(\theta,-d)$$

Where

$$S^{n}(\theta,z') = \sec\theta\int_{-d}^{z}dz'\exp\left(-\sec\theta\int_{z'}^{z}\overleftrightarrow{\kappa_e}(\theta,z'')dz''\right)\int_{0}^{\frac{\pi}{2}}d\theta'\sin\theta'\left[\vec{P}(\theta,\theta',z')\vec{T}_u^{n-1}(\theta',z') + \vec{P}(\theta,\pi-\theta',z')\vec{T}_d^{n-1}(\theta',z')\right]$$

And

$$W^{n}(\theta,z) = \sec\theta\int_{z}^{0}dz'\exp\left(-\sec\theta\int_{z}^{z'}\overleftrightarrow{\kappa_e}(\theta,z'')dz''\right)\int_{0}^{\frac{\pi}{2}}d\theta'\sin\theta'\left[\overleftrightarrow{P}(\pi-\theta,\theta')\vec{T}_u^{n-1}(\theta',z) + \overleftrightarrow{P}(\pi-\theta,\pi-\theta')\vec{T}_d^{n-1}(\theta',z)\right]$$

The solution of the downward and upward brightness temperatures is the sum of the multiple orders:

$$\vec{T}_u(\theta,z) = \vec{T}_u^{0}(\theta,z) + \vec{T}_u^{1}(\theta,z) + \vec{T}_u^{2}(\theta,z) + \cdots$$

$$\vec{T}_d(\theta,z) = \vec{T}_d^{0}(\theta,z) + \vec{T}_d^{1}(\theta,z) + \vec{T}_d^{2}(\theta,z) + \cdots$$

The iteration continues until the increment of the next order is smaller than 0.3K.

The brightness temperature that is measured by a radiometer at the observation angle θ_{ob} is then

$$\vec{T}(\theta_{ob}) = (1 - r_{10}(\theta))\vec{T}_u(\theta, z = 0)$$

2.2 Full-wave simulations for the aquifer permittivity

A key aspect of the model is the relative permittivity of the aquifer layer, for which a full wave approach is used. Full wave simulation refers to the numerical solutions to Maxwell equations. A firn is a complex, porous structure formed as meltwater percolates down to the deeper part of the firn and fills the space between the ice. In Huang et al. 2024, a computer-generated bi-continuous medium is used in Monte Carlo full-wave simulations to study the effective permittivity of an aquifer. A brief review of the method is presented here.

Consider Figure 2, in which two problems are solved to evaluate the effective permittivity. The random media to be evaluated is truncated into a sphere, as in Figure 2(A). Due to the randomness of the media, several samples of the bi-continuous modeled firn aquifer structure are generated. The scattered waves and absorption for the random structure samples are calculated to evaluate the scattering and absorption coefficients, Q_{scat}^{A} and Q_{a}^{A} respectively. In Figure 2, the white and black areas represent ice and water, respectively.

https://doi.org/10.5194/egusphere-2024-2395
Preprint. Discussion started: 31 January 2025

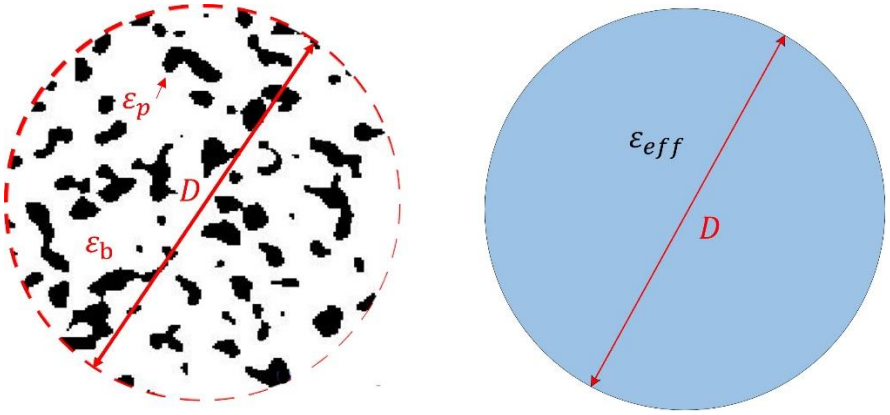

Figure 2 Problem A(left) and Problem B(right) to be solved to evaluate effective permittivity.

Notice that the scattering and absorption from problem A are evaluated based on the average scattering and absorption from the computer-generated samples, which are obtained by the following:

$$Q_{abs}^{A} = \langle \frac{k}{\pi(D/2)^2} \int \epsilon''(\vec{r}) |E_{int}(\vec{r})|^2 dV \rangle$$

$$Q_{scat}^{A} = \frac{1}{\pi\left(\frac{D}{2}\right)^2} \int_0^{4\pi} \left|\langle f_{pp}(\theta_s, \phi_s)\rangle\right|^2 + \left|\langle f_{qp}(\theta_s, \phi_s)\rangle\right|^2 d\Omega$$

Where the angular bracket ⟨ ⟩ stands for a Monte Carlo ensemble average over the samples. $E_{int}(\vec{r})$ is the internal field inside the mixture. f_{pp} and f_{qp} are the scattering amplitudes for p-polarized incident waves, with the scattered waves being p and q-polarized. In the linear polarization basis, p and q can both represent H and V. For the mixture of water and ice in the aquifer, in the L band, water has much higher dielectric loss. The absorption loss due to ice can thus be ignored.

In problem B, the scattering and absorption cross-section (Q_{SCAT}^{B} and Q_{abs}^{B}) of a homogeneous sphere are solved. The sphere's diameter in Problem B is the same as the artificial boundary in Problem A. The calculations are based on the analytical Mie scattering theory. Q_{scat}^{B} and Q_{abs}^{B} are compared with Q_{scat}^{A} and Q_{abs}^{A} . The real and imaginary parts of problem B are adjusted until $Q_{scat}^{B} = Q_{scat}^{A}$, $Q_{abs}^{B} = Q_{abs}^{A}$ The effective permittivity of the mixture is considered to be the value of the adjusted permittivity.

In this research, the aquifer's liquid water contents range from 5% to 25%. The values are obtained through full-wave simulation using bi-continuous media with $\langle\zeta\rangle = 11000$ and b=5, which correspond to an effective particle size of 1mm. A detailed discussion of the simulation process can be found in Huang et al. 2024. In the dry firn, the density profile is converted into the permittivity profile from the work of Matzler 1996 and Tiuri 1984.

Results from the radiative transfer model combined with the aquifer effective permittivity were computed for the three sites of interest using the available in-situ data. The region above the aquifer is assumed to be dry snow.

https://doi.org/10.5194/egusphere-2024-2395
Preprint. Discussion started: 31 January 2025

3. Results

3.1 Time series modeling for Greenland and Antarctica

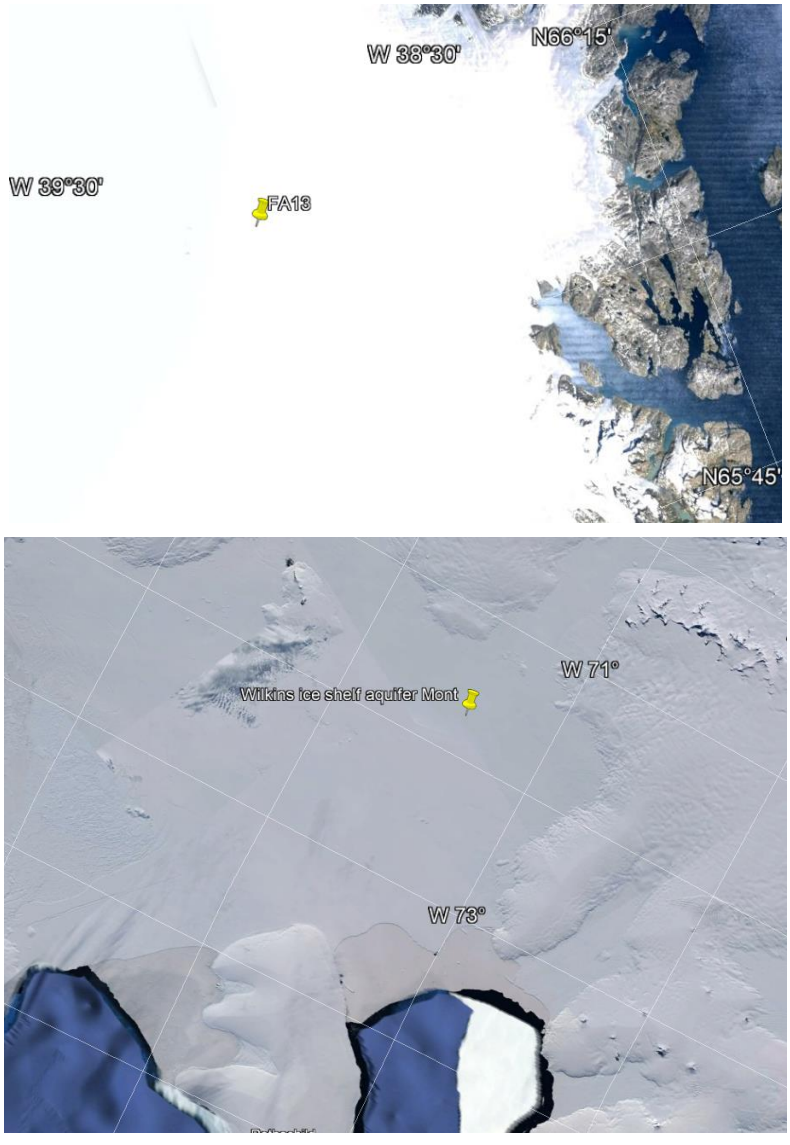

Figure 3 Borehole locations The borehole is near the southeast coast of Greenland, and the borehole study on Antarctica is on the Wilkins Ice shelf.

The borehole locations are presented in Figure 3 for Greenland and Antarctica, respectively. Both of the two locations are close to the ocean coast.

https://doi.org/10.5194/egusphere-2024-2395
Preprint. Discussion started: 31 January 2025

3.1.1 temperature and density in situ measurements

In situ measurements of physical temperature and firn density are plotted in Figures 4-5 for the Greenland and Antarctic sites, respectively.

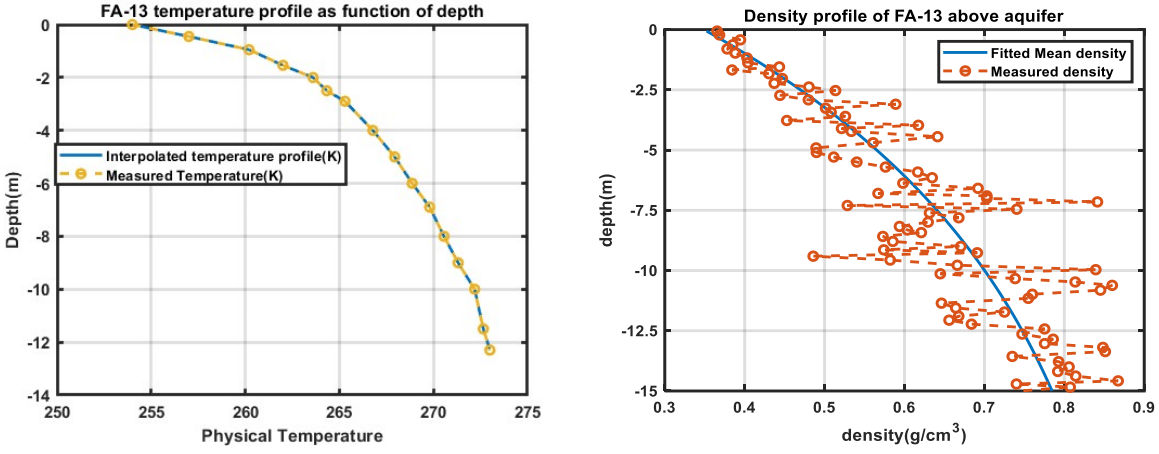

Figure 4 Temperature(left) and density profiles of FA13 from [Koenig et al. 2014, and Montgomery et al. 2018]. The measurements are taken on a scale of 0.5 meters.

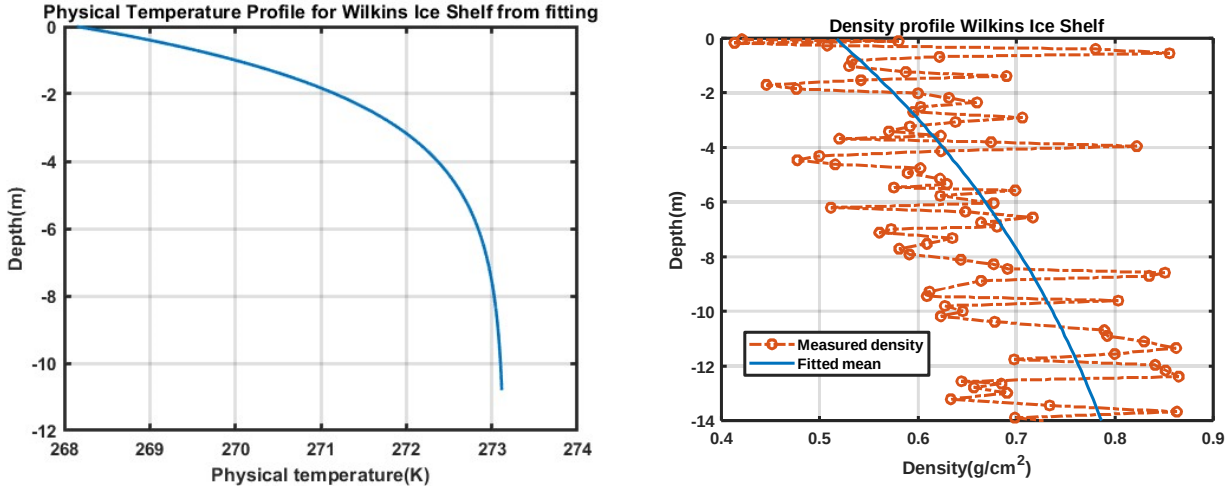

Figure 5 Density profile from the borehole in Wilkins Ice Shelf and the fitted temperature connecting surface and water table. The temperature profile is composed of the surface temperature and the water table depth.

For the borehole of FA-13 in Greenland, the water table location (upper boundary of the aquifer) is available from the GPR echogram from the Accumulation Radar survey performed in 2014. The FA-13 borehole was drilled and studied in 2013. Density measurement and water table location are available from the Wilkins Ice Shelf's borehole (Figure 5). The physical temperature in the borehole is not publicly available. As the radiative transfer model needs a temperature profile as input, a fitted temperature profile is generated using the surface temperature and water-ice mixture profile. The density and temperature profiles are plotted in Figures 5 and 6.

https://doi.org/10.5194/egusphere-2024-2395
Preprint. Discussion started: 31 January 2025

For FA-13, the temperature profile smoothly increases from 254K at the firn-air interface to 273.15K at the dry firn aquifer interface. This indicates that the top layer contains no liquid water before reaching the water table since the temperatures are below the melting point. For the Wilkins location, the function A-Bexp(-Cz) is used to connect the surface and aquifer temperatures. In the forward simulation, the physical temperature in the dry firn region is obtained as follows: Assume that the mean surface temperature is at -5℃ and the temperature profile follows an exponential-like function as $T(z) = 273.15 - 5exp(bz)$. The b value can be obtained by forcing $T(z = -13.5) - 273.15 < 10\text{^} - 3$. The results show that setting b, being one-fifth of the water table depth, which is b=2.65m, would fit the need.

For the density profiles, the mean density is obtained by fitting a function of the shape $C - Dexp(-Ez)$ to the measured data. The density profiles show properties that are very different from those in the inner part of Greenland or Antarctica. Instead of having a slowly increasing mean density, as shown in the borehole measurements where the mean profile reaches the critical density of 0.55g/cm^3 at about 15m down from the surface, the mean density profiles in the aquifer regions increase dramatically. The density can be as high as 0.8g/cm^3 at a depth of 12m, as shown in the case of FA13. The magnitude of density fluctuations is also much higher than those in the accumulation zone of Greenland and Antarctica. In terms of the density variations, the density fluctuates dramatically from the mean value due to the presence of refrozen ice structures in these regions.

The water level for all the boreholes used in this research is presented in Table 1. The positions of FA-13 and Wilkins Ice Shelf are from the borehole measurements. The location (66.19N,39.1685W) and the water table depth are estimated from the Accumulation Radar echogram taken in 2014. The corresponding echogram is provided in Appendix B.

Table 1 Water Table levels for all three locations

Positions	FA13(66.1812N, 39.0435W)	66.19N,39.1685W	Wilkins Ice Shelf(−70.80S, −71.71W)
Water table depth from surface(m)	12.5	15.5	13.6

3.1.2 Effective permittivity of firn aquifer

The effective permittivity values for the mixture are important factors affecting the emission. The contrast between the effective permittivity of the aquifer and the dry firn above the aquifer determines the reflected amount of thermal emission into the aquifer. Figure 6 provides the effective permittivity of the aquifer (ice water mixture) as a function of liquid water content. The three curves correspond to different shapes of inclusions, such as spheres, bicontinous media(shapeless), and needles. Maxwell-Garnett mixing formula is used to evaluate the sphere and needle cases, while the bicontinous media is evaluated using the method in section 2.2. As shown in the plots, both the real and imaginary parts of effective permittivity values increase with respect to the increase in liquid water content. However, the speed of the increase is very different.

https://doi.org/10.5194/egusphere-2024-2395
Preprint. Discussion started: 31 January 2025

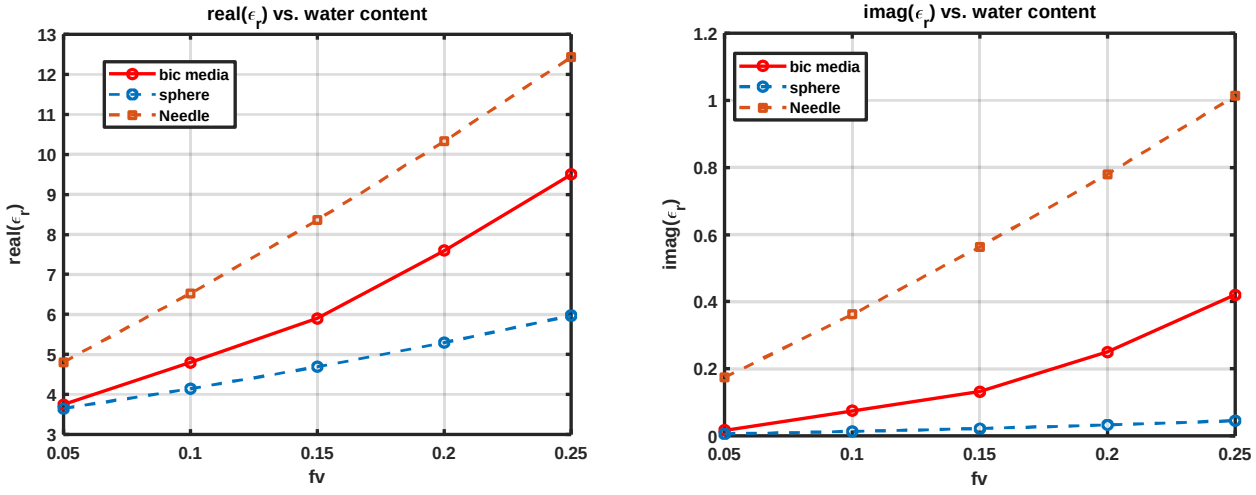

Figure 6 Effective permittivity values through the full wave bi-continuous media and spheres

Medium with sphere inclusions has the lowest permittivity values in both the real and imaginary parts. The increments are also the smallest in all three cases. For the real and imaginary parts, the values increase from 3.65 to 5.97 and from 0.006 to 0.045 as water content increases from 0.05 to 0.25. Needle inclusion has the largest values and the largest increments. The values increase from 4.8 to 12.4 and 0.17 to 1.01 for the real and imaginary parts, respectively. The bicontinous media is between the two, with an increase from 3.75 to 9.5 and 0.017 to 0.42 for the real and imaginary parts, respectively. This indicates that effective permittivity depends highly on the shape of the inclusion. A good geometry description of the mixture in permittivity modeling is important in modeling the emission.

3.1.3 Forward simulation of SMAP brightness temperatures

Time series results for FA13 are provided in Figure 7. The numerical simulation is performed for five points in the time series from Dec 7th, 2015, to early April 2016. Melting events occur in the later days of April. Thus, the later part of the time series is not discussed. The parameters we used for the five-time series points are listed in Table 2.

The temperature profiles and water table location are provided in the top two plots in Figure 7. At the beginning of the time series, early December 2015, the water table is assumed to be half of the depth of April 2016. As spring of 2016 came, the water table gradually decreased to its lowest location of 12.3m from the surface. Regarding the temperature profile, at each time point, the temperature profile in April is "squeezed" to fit the temperature at the dry firn aquifer interface.

As in Figure 4, the mean density profile is used as input for the iterative approach. The density fluctuation properties are used as a tuning parameter. For this case, a density standard deviation of 0.088g/cm^3 is used with vertical and horizontal correlation lengths of 8.5cm and 20cm, respectively. The statistical properties of the density fluctuations are considered to be homogeneous from the top to the bottom of the dry firn.

https://doi.org/10.5194/egusphere-2024-2395
Preprint. Discussion started: 31 January 2025

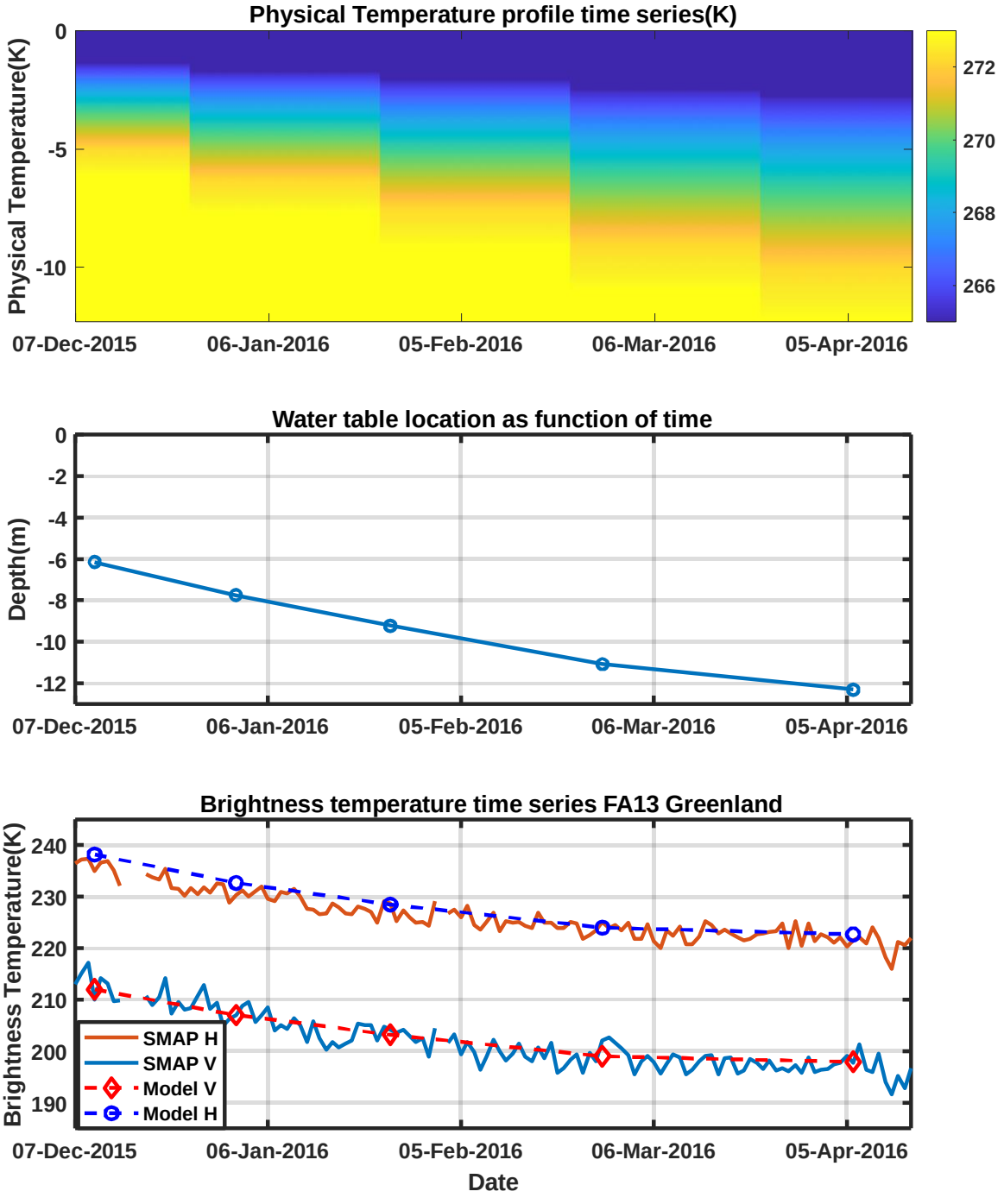

Figure 7 Time series for FA13 from winter 2015 to summer 2016. The match-up stopped in early April 2016.

https://doi.org/10.5194/egusphere-2024-2395
Preprint. Discussion started: 31 January 2025

270

Table 2 FA-13 parameters for the 5 points of time series in forward simulations of TB For Greenland

		Early Dec 2015		Jan		3Feb		March		Early April	
Dry firn thickness(d)(m)		6		7.75		9.2		10.76		12	
Aquiferϵ_r(10%lwc)		7.26+0.25i		7.26+0.25i		7.26+0.25i		7.26+0.25i		7.26+0.25i	
firn permittivity adjacent to the aquifer		2.25		2.36		2.47		2.59		2.65	
Dry firn density variations		$Std(\rho) = 0.088 g/cm^3$,$l_z = 8.5cm$, $l_\rho = 20cm$									
		V	H	V	H	V	H	V	H	V	H
TB modeled time series		234.97	209.75	230.7	206.2	227.43	203.44	224	201	222.8	199.5
TB reduction: 273-Model(K)		34.8	61	40.3	66	44.5	70	49	74	50.2	74.5
TB reduction	Firn+snow Air interface	21.8	34	28	43	33.8	49.6	39.5	56	40.7	57.5
	Snow -air interface	13	27	12.3	23	10.7	20.4	9.5	18	9.5	17

https://doi.org/10.5194/egusphere-2024-2395
Preprint. Discussion started: 31 January 2025

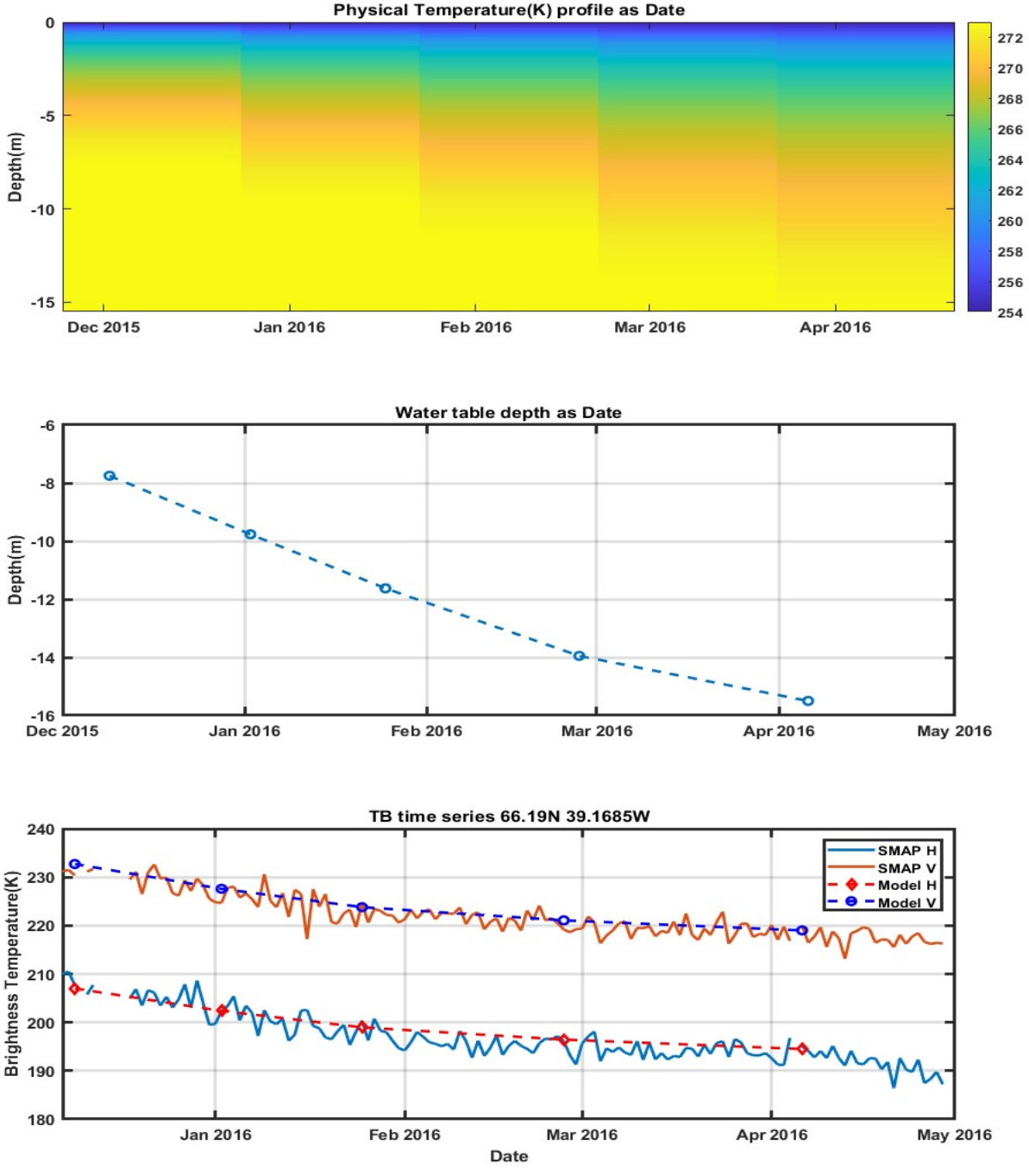

Figure 8 Time series forward modeling of Brightness temperature at location 66.19N 39.1685W. The mean density profile is obtained from FA-13. The physical temperature profile uses the FA-13 profile but is adjusted to have a slower changing speed according to depth. The water table location is obtained by the GPR echogram by KU's Accumulation Radar.

https://doi.org/10.5194/egusphere-2024-2395
Preprint. Discussion started: 31 January 2025

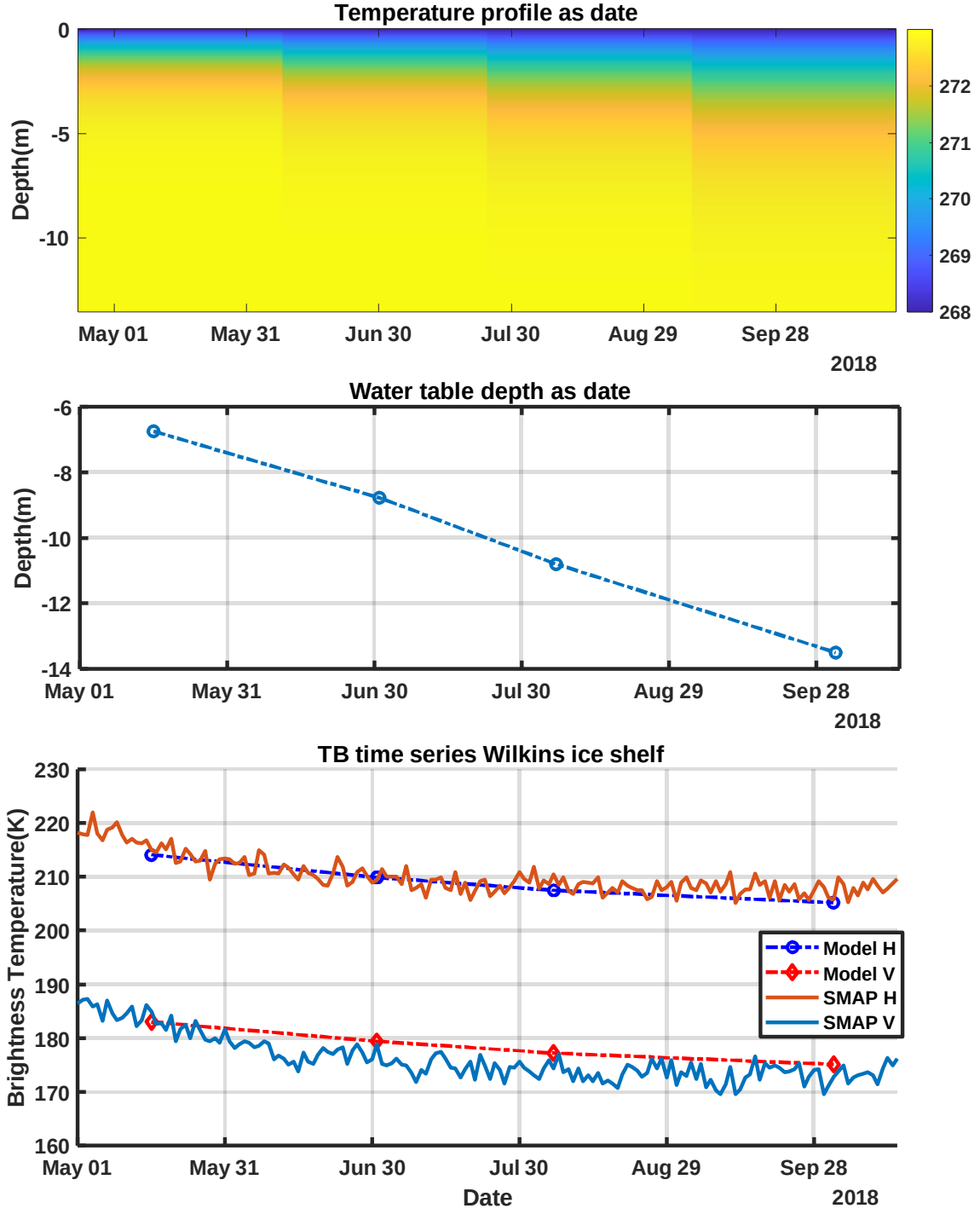

Figure 9 Brightness temperature time series data and forward modeled results over the borehole pixel in Wilkins Ice shelf, 2018.

https://doi.org/10.5194/egusphere-2024-2395
Preprint. Discussion started: 31 January 2025

The firn aquifer permittivity is set as 7.6+0.25i, corresponding to 20% of liquid water content for the water and ice mixture in the firn aquifer. The results are obtained from the full wave simulations using bi-continuous media, as in Figure 6. In the time series simulations, the permittivity of the region below the water table is assumed to be the same for all the data points where forward simulation is performed.

Table 3 Density fluctuation parameters and the aquifer permittivity for the forward match-up results of FA-13 in Figure 7

	Value
$std(\rho)$	$0.088 g/cm^3$
l_z	$8.5cm$
l_ρ	$20cm$
$\epsilon_r^{aquifer}$	$7.6 + 0.25\mathrm{i}$

With the given density parameters, the simulated time series matches the measured brightness temperatures for both V and H polarizations. The overall standard deviation is around 3K. A detailed analysis of the contribution to the brightness temperature reduction in terms of reflectivity is provided in Table 2. In the analysis, the depth of the water table decreases from 6m in early December from the surface to 12.3m in early April. As the water table lowers, the dry firn volume increases. As indicated in the table, reduction from the aquifer interface decreases. This can be explained by the change of firn permittivity adjacent to the aquifer. The permittivity of dry firn above the aquifer changes from 2.25 to 2.65. The permittivity difference between the aquifer and the dry firn is thus decreased. A major reduction in the emission is due to the density fluctuations in the dry firn. As the depth increases, dry firn volume increases, leading to an increase in reflection numbers due to density fluctuations. The brightness temperature reductions can be explained by the increase in the dry firn volume. Notice that when modeling the time series, the mean density profile is fixed. The change of the water table would 'truncate' the mean density profile that holds the variations.

The time series analysis is also performed for the second location in Greenland. The brightness temperature time series are plotted with the forward-modelled brightness temperature in Figure 8 at the same time spot as in Figure 7. For this location, it is still assumed that the water table depth is changing. This location is about 6km away from the FA-13. For such a distance, the mean density profile in this location is assumed to be the same as FA-13. The temperature profile in FA-13 is scaled according to the depth for this location. So, the melting point is at the water table depth. In the time series from Dec to April, the water table depth changes in terms of percentage of the total depth are the same as the FA-13. The physical temperature profile is thus changed accordingly by compressing the profile according to depth. The parameters used for the simulation are provided in Table 4. A 10% water content is used for the simulation. Density variation properties are also listed in Table 4. The results show good agreement with the time series data for both V and H pol. Results in this location indicate that the density properties may not change significantly within some distance.

https://doi.org/10.5194/egusphere-2024-2395
Preprint. Discussion started: 31 January 2025

Table 4 Density fluctuation parameters and the aquifer permittivity for the forward match-up results in Figure 9

	Value
$std(\rho)$	$0.088 g/cm^3$
l_z	$7.8cm$
l_ρ	$20cm$
$\epsilon_r^{aquifer}$	$4.8 + 0.05\mathrm{i}$

The last time series analyzed is the SMAP measurements taken over the Wilkins Ice Shelf in Antarctica starting in May and ending in mid-October.

Based on the in situ measurement from the borehole and the GPR survey over those areas, the water table is 13.5m from the snow-air interface. As shown in Figure 9, the measured brightness temperature over the Wilkins ice shelf is much lower than the observations over Greenland. The typical brightness temperature of H pol in Greenland is usually above 180K, while for the observations in Wilkins Ice Shelf, the H pol measurements are around 173K. The lower brightness temperature could be due to the higher density fluctuations and the higher water content in the aquifer.

To forward simulate the brightness temperature for the time series points, the water table location is adjusted as shown in Figure 10. The properties are used to characterize the density fluctuation properties to match up both the V and H pol brightness temperatures:$std(\rho) = 0.13 g/cm\text{^}3$, $l_z = 4cm$,$l_\rho = 16cm$. The forward simulated results are plotted together with the SMAP measurements. The simulated results reflect the decrease in brightness temperature, assuming the changes are purely due to the changes in the water table.

Table 0-5 Density fluctuation parameters and the aquifer permittivity for the forward match-up results in Figure 10 for the Wilkins Ice shelf

	Value
$std(\rho)$	$0.13 g/cm^3$
l_z	$4cm$
l_ρ	$16cm$
$\epsilon_r^{aquifer}$	$7.26 + 0.25\mathrm{i}$

3.2 Parameter Sensitivity Analysis

In this section, the FA-13 site is used as an example to analyze the sensitivity of brightness temperature to liquid water content in the firn aquifer. Brightness temperatures at 40 degrees are calculated for different aquifer water table depths and liquid water content.

Brightness temperatures as a function of liquid water content in the aquifer are plotted in Figure 9. Each subfigure corresponds to a different water table depth from the surface, starting from 6.15 m (half of the maximum depth) to 12.3 m (maximum depth)

https://doi.org/10.5194/egusphere-2024-2395
Preprint. Discussion started: 31 January 2025

below the firn-air interface. When performing the simulations, the volume scattering from the dry firn is characterized using. $std(\rho) = 0.088g/cm\text{^}3$, $l_z = 0.085m, l_\rho = 0.2m$, which is the same as the parameters used for the time series match-up.

All brightness temperature plots show a decreasing trend with the increased liquid water content inside the aquifer. However, the impact of liquid water content decreases as the water table depth increases. When the water table is 6.15 m below the surface, the brightness temperatures decrease by 8K in H pol and 10K in H pol as the liquid water content increases from 5% to 25%.

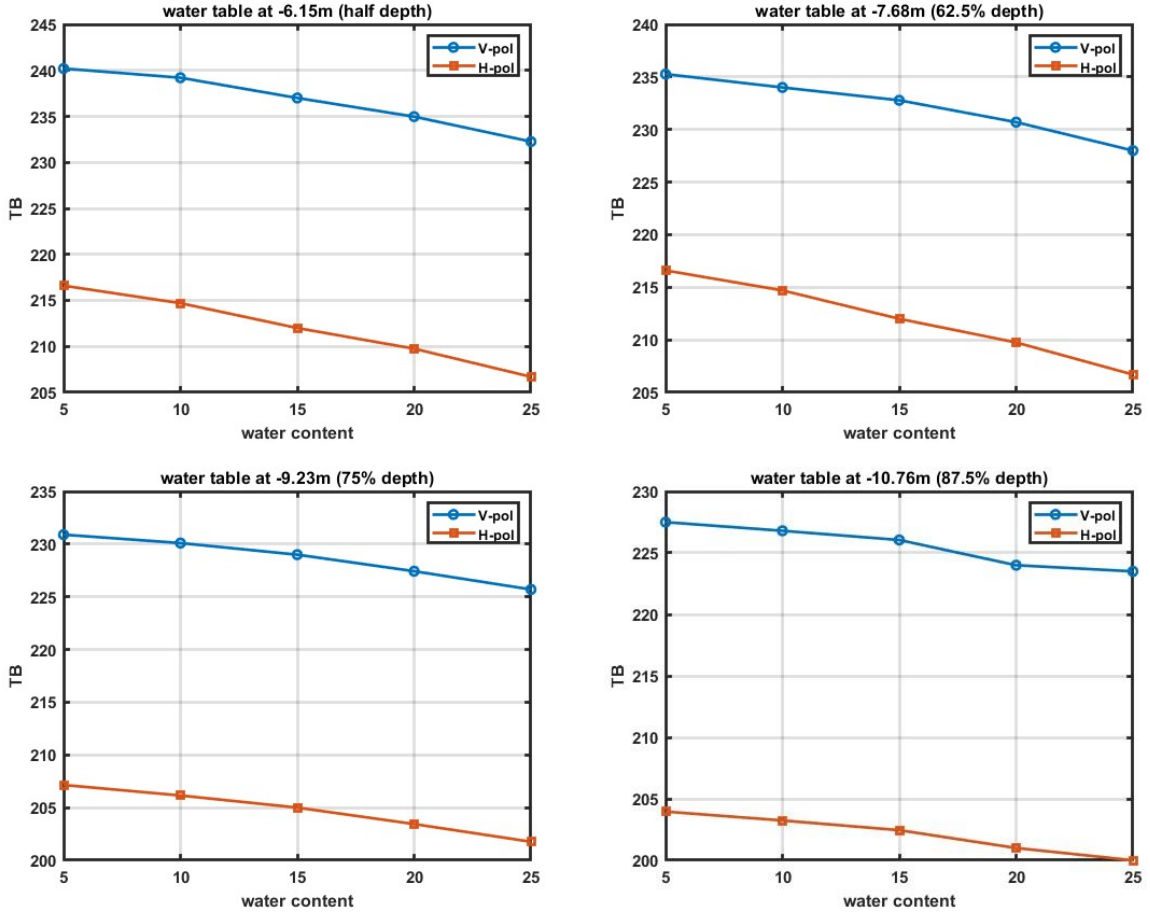

https://doi.org/10.5194/egusphere-2024-2395
Preprint. Discussion started: 31 January 2025

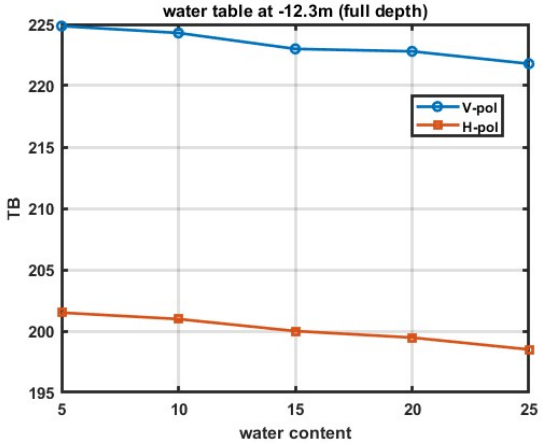

Figure 10 Brightness temperature as a function of liquid water content in firn aquifer with water table at different depths.

Then, for water table depth at 7.68, 9.23, and 10.22 m, the brightness temperature decreased by 7.2K, 5.4K, and 4K for V-pol, and 7.3K, 5.4K, and 4K for H-pol, respectively. The changes in brightness temperature finally become 3K and 3.3K when the aquifer water table depth is 12.3 m. This phenomenon happens due to two factors: 1. The decrease of permittivity contrast between the dry firn and aquifer. The permittivity of the aquifer is fixed as the liquid water content is fixed. However, the firn permittivity increases when depth increases due to the increase in mean density. The second factor is the increase of volume scattering in the dry firn region—the total volume scattering increases as more scatterers are included due to the increase in depth.

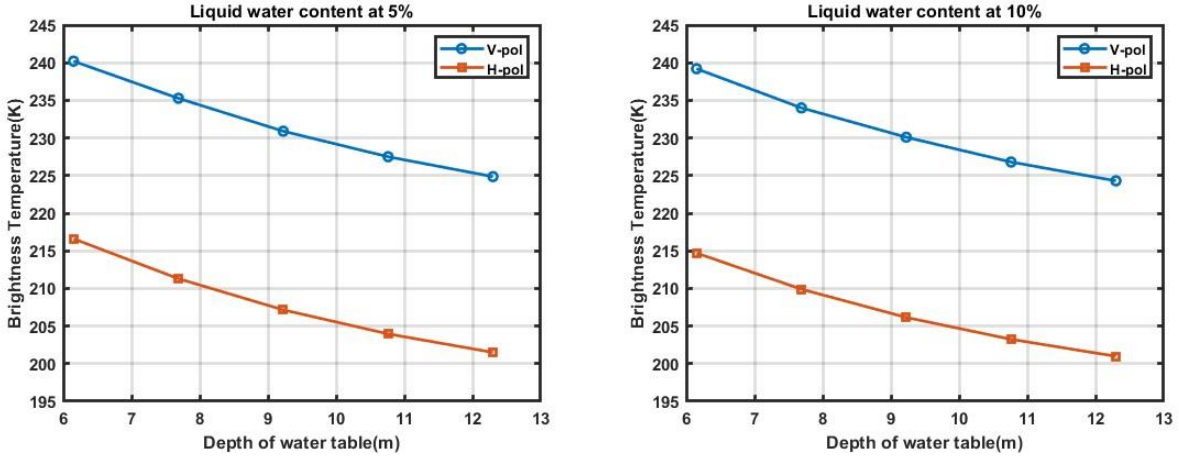

https://doi.org/10.5194/egusphere-2024-2395
Preprint. Discussion started: 31 January 2025

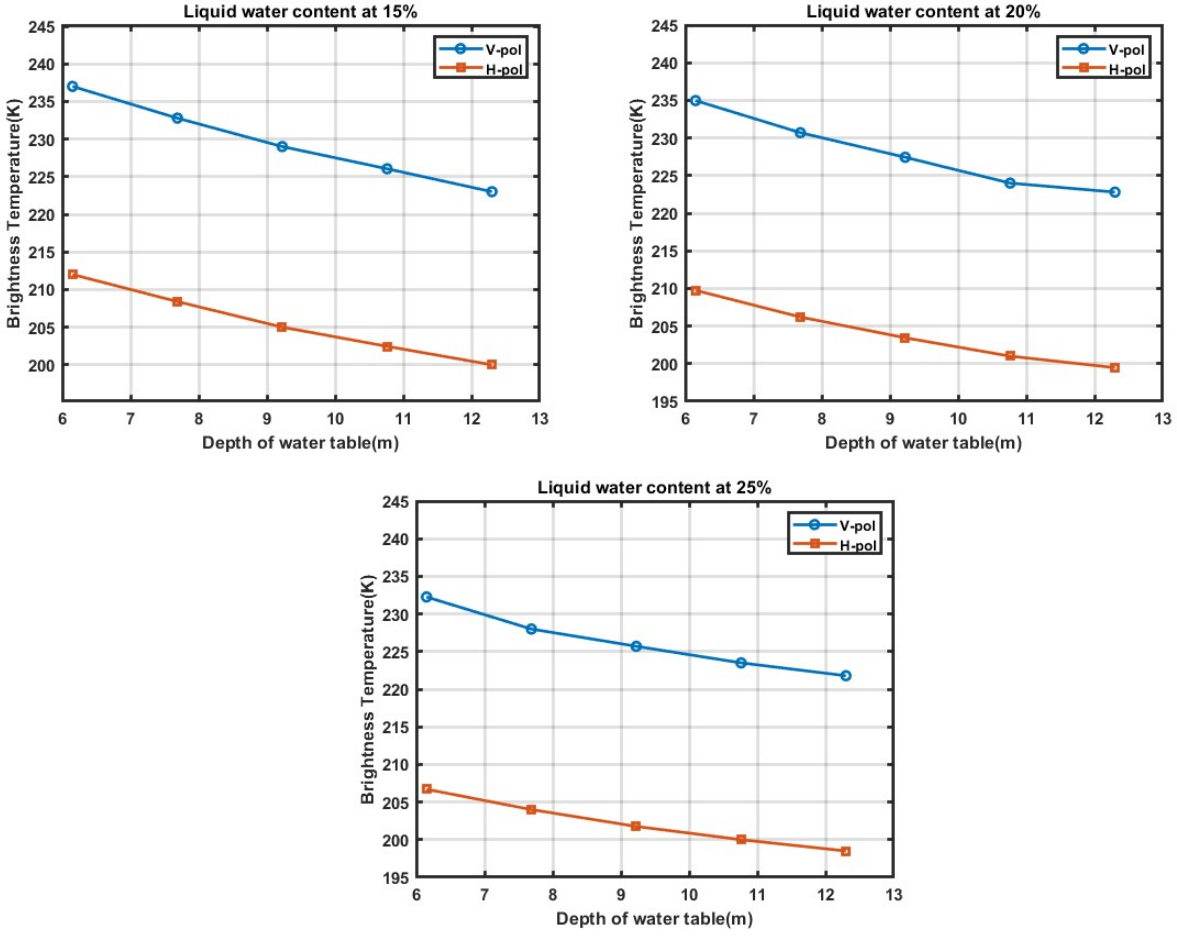

Figure 11 Brightness temperature changes as a function of water table depth at different fixed liquid water contents

Brightness temperature changes as a function of depth are plotted in Figure 11 for fixed aquifer liquid water content. For all the cases, as the water table depth changes from 6.15 to 12.3 m, the decrease in brightness temperatures is usually more than 10K for both V and H pol. The most significant drop in brightness temperature happens for liquid water content of 5%. The brightness temperature drops from 240K to 225K for V-pol and 216.6K to 201.5K. At 25% liquid water content in the aquifer, the brightness temperature drops about 10K when the water table changes from 6.15 to 12.3 m. The dynamic range decreases as the liquid water content increases. This is due to the increase of multiple reflections happening between the top and bottom interfaces of the dry firn region.

The combined effects of water content and water table depths are presented in this section with the following two combinations: 1. Increasing liquid water content in the aquifer as the water table goes deeper. 2. Decreasing the liquid water content in the aquifer as the water table goes deeper. It is unclear how the liquid water content would change according to the seasonal changes. These results illustrate the two possible trends of liquid water content from winter to spring. The simulation results would provide a physical intuition for interpreting the time series data.

https://doi.org/10.5194/egusphere-2024-2395
Preprint. Discussion started: 31 January 2025

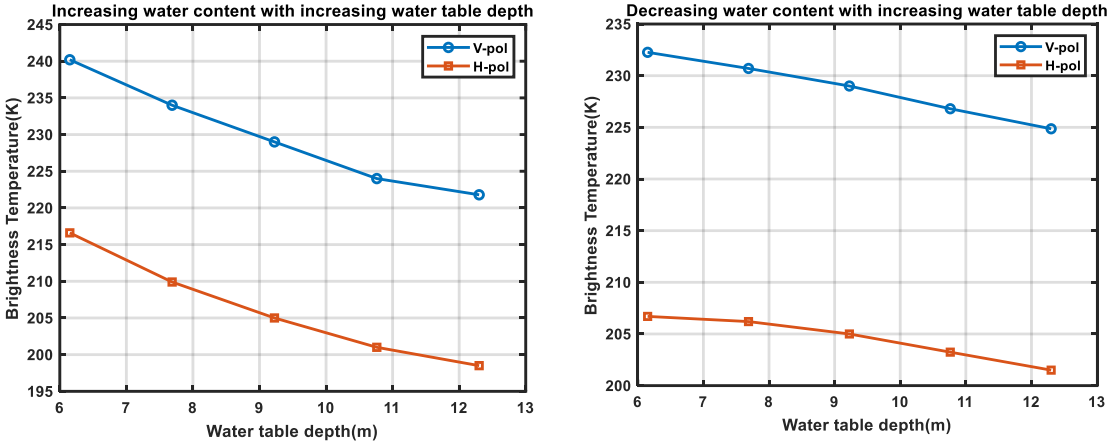

Figure 12 Brightness temperature changes as a function of depth with the liquid water content in an increasing and decreasing order. For the left-hand side figure, liquid water content increases from 5% to 25% from 6.2 to 12.3m water table depth. For the right-hand side figure, liquid water content decreases from 25% to 5% as the water table depth increases.

Figure 12 plots brightness temperatures for the cases when the liquid water content increases and decreases with respect to the water table depth. The left figure shows the case where liquid water content increases as water table depth decreases. As can be observed from the figure, the increased water content contributes constructively to the decreased water table depth. The overall effect contributed to a 20K reduction in V-pol and an 18K reduction in H-pol. On the other hand, for the righthand side figure, the decreasing water content counters the effects of the increasing depth. The overall effects decrease the change of brightness temperature with respect to depth. The V-pol decreases by 7k, and the H-pol decreases by only about 5K in total. The parameters of $std(\rho), l_z$ and l_ρ are the parameters that control the properties of volume scattering in the dry firn.

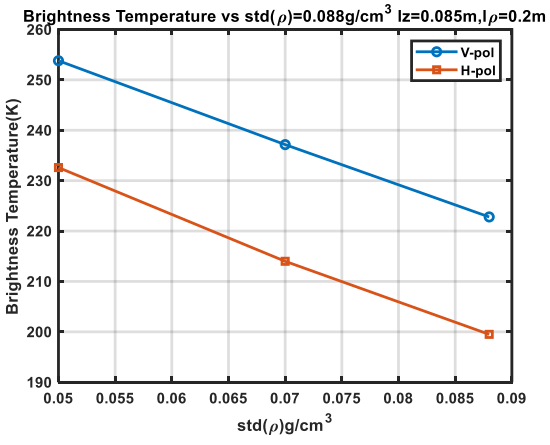

Figure 13 Brightness temperature change with respect to std(ρ) V-pol and H-pol both decrease as the value of std(ρ) Increases.

https://doi.org/10.5194/egusphere-2024-2395
Preprint. Discussion started: 31 January 2025

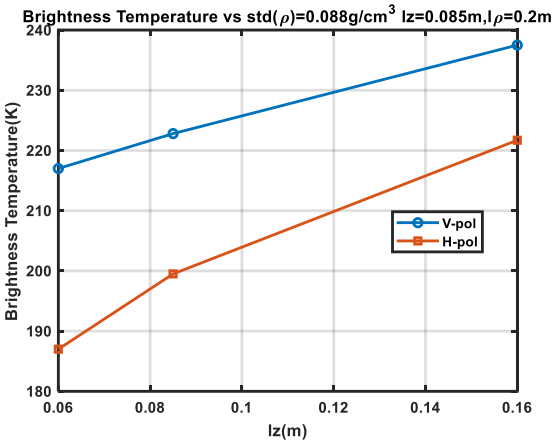

Figure 14 Brightness temperature changes with respect to lz. With smaller lz, the reduction to brightness temperature gets stronger.

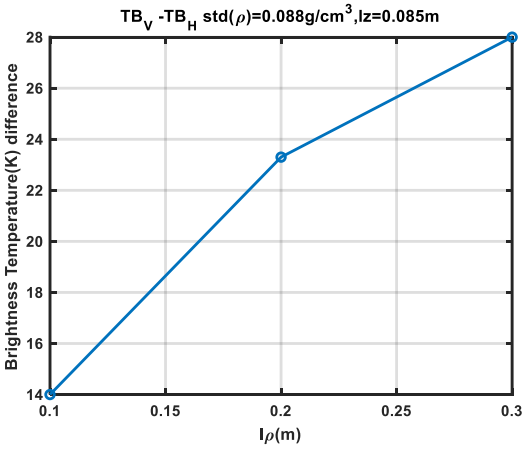

Figure 15 The brightness temperature difference between V and H pol with respect to horizontal correlation length.

The parameters of $std(\rho)$ and l_z are determining the strength of each reflection and the number of reflections in a unit length in the z-direction. As shown in Figure 13 and Figure 14, the increase of $std(\rho)$ and the reduction of l_z would reduce the brightness temperature in both V and H pol. The horizontal correlation length controls the difference between V-pol and H-pol emission, as shown in Figure 15. The increase of l_ρ would make the media behave more likely to layers, making the V-pol and H-pol more different from each other. Smaller l_ρ values allow the V-pol and H-pol to be coupled to each other.

4. Discussion

First, the simulation results provided the predictions of aquifer permittivity values based on different assumptions for the shapes of water inclusions in the aquifer. The modeled permittivity values have shown significant differences between each

https://doi.org/10.5194/egusphere-2024-2395
Preprint. Discussion started: 31 January 2025

other and have also shown different dependence on the changes in liquid water content in the mixture. This fact indicates the strong permittivity dependence on the inclusion shapes. Physically, the water inclusions in the aquifer are formed by liquid water, filling the gaps between the ice structures. These gaps usually have no definite shapes as spheres or ellipsoids. The bicontinous media has the ability to simulate such shapeless structures, which indicates a better way of characterizing the effective permittivity of the firn aquifer. The current simulated effective permittivity values of the firn aquifer are calculated based on the setup of $\langle\zeta\rangle$=11000 and $b = 5$, which corresponds to a mean structure size of 1mm. The characterization of the firn aquifer's effective permittivity can be benefited from the microstructure study on the firn aquifer.

Secondly, the radiative transfer model provided in this paper has shown its ability to predict the time series brightness temperature changes from winter to early spring before surface melting starts for both the V and H pol time series brightness temperatures. This model eliminates the ambiguity in the previous 1D random layering structure model, where different parameters are needed to explain the different polarized brightness temperature data. For future work on the retrieval of liquid water content for the top region of the aquifer, this model enables the use of both V and H pol measurements.

In comparison with the time series results from Greenland and Wilkins Ice Shelf, Antarctica, it can be observed that the brightness temperatures from Wilkins Ice Shelf are about 10K lower than the TB observed over southeast Greenland. Our analysis provides one of the possibilities that is assuming the firn aquifer in the Wilkins Ice Shelf has a higher liquid water content and a higher density variation. The selection of higher density variation than Greenland can be justified by the comparison of density profiles in the first section. The usage of higher liquid water content in the aquifer for the Wilkins Ice Shelf needs further validation.

In Figure 7, the time series is simulated based on the assumption of unchanged liquid water content in the firn aquifer and density parameter with a changing depth of the firn aquifer. In Figure 14The simulated brightness temperatures are based on the same density parameters but include changes in the liquid water content. If the liquid water content in the aquifer has a decreasing trend, the brightness temperature from December to April is much less than the case when the liquid water content increases with time and the change in Figure 7. This shows that the change in the liquid water with respect to time can also influence the time series brightness temperature at the L-band.

The model used in this paper has assumed a dry condition above the aquifer. The current model does not cover the case when liquid water is present above the aquifer. Figure 16 shows the temperature profiles measured in the boreholes of FA 15-1 and -2. This is different from the case in FA-13, where the temperature profiles reach 0℃ at the position of the water table. The temperature profiles in these two boreholes reach 0℃ at a much shallower position than the water table. As a result of this, there is a "warm" region. The high temperatures in these regions allow the existence of liquid water. These regions are called unsaturated zones in the work of [Miller et al. 2017]. The thermal emission from these regions is much more complicated since the liquid water content in these regions will affect the contribution from the aquifer. With higher liquid water, radiometers may not see emissions from the aquifer. Further studies are needed to understand the loss factor of the unsaturated zone, where the media is a three-phase mixture of air, ice, and water. A method of separating the regions with and without unsaturated zones is needed in order to apply the physical model presented in this paper.

https://doi.org/10.5194/egusphere-2024-2395
Preprint. Discussion started: 31 January 2025

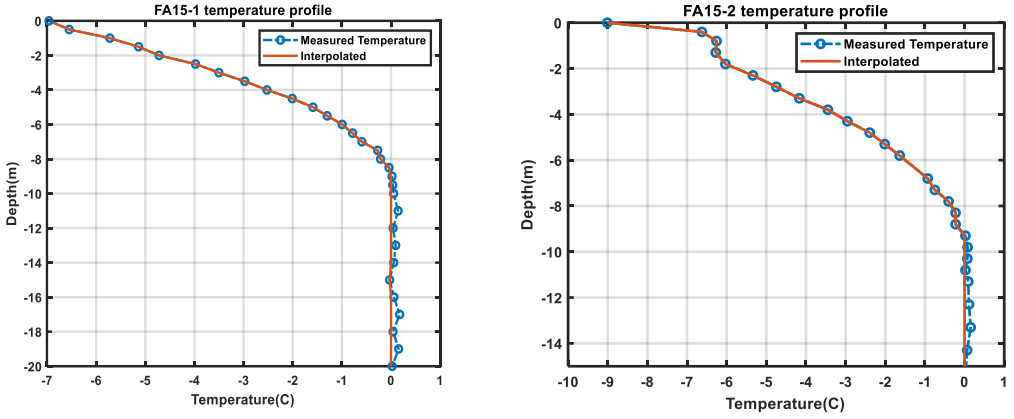

Figure 16 Temperature(left) of FA15-1 and FA15-2 [O.Miller et al. 2017]. The water table locations are -19.8m and -14.4m respectively. Unlike what is observed in FA-13, where the physical temperature becomes 0℃ at the interface of the dry firn and aquifer, the physical temperature profiles in these two boreholes reach 0℃ before reaching the aquifer water table.

One of the features that could affect the emission is the mean density profile of the firn. The mean profile affects both the reflections due to the dry firn and the interface of dry firn and aquifer. Several different mean density profiles need to be used in the simulation to evaluate its effects. However, the in situ data is very limited. Another approach is to use the simulated profiles. The Community Firn Model[Stevens et 2021] has been updated lately to better deal with the percolation facets of the polar ice sheet. However, the simulated mean density profile reaches the ice density at a much shallower depth than the measured mean density, which does not correctly reflect the truth. The modeled results need to be further improved before using it to analyze the mean density profile effects.

As discussed earlier in the paper, the variation properties of the dry firn affect the emission. These properties need to be characterized. A possible approach is to use the data from higher frequency microwave sensors, such as the AMSR-2 multi-frequency radiometer data at C, X, Ku, and even Ka Bands.

5. Conclusions

A physical model for the L-band microwave thermal emission of a firn aquifer region was reported. The radiative transfer model formulation is solved iteratively to include scattering contributions within the inhomogeneous dry firn region. The reflections of thermal emission are considered due to the firn-aquifer interface, air-firn interface, and density fluctuations in the dry firn region. A full wave approach also was used to simulate the effective permittivity of the aquifer. The 3D structure of the modeled density fluctuations allowed both V and H-polarized SMAP measurements to be reproduced using a single set of parameters and to reproduce SMAP time series data over the Greenland coast and Wilkins Ice Shelf, Antarctica.

Sensitivity analyses further show that the L-band brightness temperature varies more strongly with aquifer liquid water content when the water table is closer to the surface. This is because the permittivity difference in the aquifer and the dry firn relatively

https://doi.org/10.5194/egusphere-2024-2395
Preprint. Discussion started: 31 January 2025

more contributes to the brightness temperature reduction. This indicates a better result in future retrieval work than in deeper aquifer cases. It is also shown that both the firn aquifer depth and the liquid water content in the firn aquifer would affect the time series brightness temperature at the L-band. The method provides a tool for the radiometry study of firn aquifer. The brightness temperatures due to different combinations of density properties and firn aquifer properties can be estimated through the model. The method can also be extended to explain the passive microwave measurements in other frequencies. The model also provides a theoretical basis for potentially retrieving firn aquifer liquid water content using passive microwave data. Look-up tables can be generated and used in future retrieval.

Appendix A. Iterative solution of radiative transfer equations

The first step is to convert the equations from differential-integral form into pure integral forms. For the upward brightness temperature, the variable z is changed into z', then the term $\exp\left(-\sec\theta\int_{z'}^{0}\overleftrightarrow{\kappa_e}(\theta,z'')dz''\right)$ is multiplied to both sides of the equation. For upward-going brightness temperatures, integration performed on z' ranges from $z'=-d$ to $z'=z$. The equation is thus changed into:

$$\int_{-d}^{z}\cos\theta_i\frac{d}{dz'}\vec{T}_u(\theta,z')\exp\left(-\sec\theta\int_{z'}^{0}\overleftrightarrow{\kappa_e}(\theta,z'')dz''\right)=$$

$$\cos\theta_i\overrightarrow{T_u}(\theta,z)\exp\left(-\sec\theta\int_{z}^{0}\overleftrightarrow{\kappa_e}(\theta,z'')dz''\right)$$

$$-\cos\theta_i\vec{T}_u(\theta,z'=-d)\exp\left(-\sec\theta\int_{-d}^{0}\overleftrightarrow{\kappa_e}(\theta,z'')dz''\right)$$

$$-\int_{-d}^{z}dz'\cos\theta_i\overrightarrow{T_u}(\theta,z')[\sec\theta\overleftrightarrow{\kappa_e}(\theta,z')]\exp\left(-\sec\theta\int_{z'}^{0}\overleftrightarrow{\kappa_e}(\theta,z'')dz''\right)$$

Integrate the left-hand side by parts and cancel out the same terms on both sides of the equation. The formatted equation becomes the following:

$$\overrightarrow{T_u}(\theta,z)=\vec{T}_u(\theta,z'=-d)\exp\left(-\sec\theta\int_{-d}^{z}\overleftrightarrow{\kappa_e}(\theta,z'')dz''\right)$$

$$+\sec\theta\int_{-d}^{z}\kappa_a(z')T_0(z')\exp\left(-\sec\theta\int_{z'}^{z}\overleftrightarrow{\kappa_e}(\theta,z'')dz''\right)dz'$$

$$+\vec{S}(\theta,z)$$

Where $\overrightarrow{S_u}(\theta,z)$ is the term that accounts for the scattering:

$$\mathrm{S}(\theta,z')=\sec\theta\int_{-d}^{z}dz'\exp\left(-\sec\theta\int_{z'}^{z}\overleftrightarrow{\kappa_e}(\theta,z'')dz''\right)\int_{0}^{\frac{\pi}{2}}d\theta'\sin\theta'\left[\vec{P}(\theta,\theta',z')\vec{T}_u(\theta',z')+\vec{P}(\theta,\pi-\theta',z')\vec{T}_d(\theta',z')\right]$$

https://doi.org/10.5194/egusphere-2024-2395
Preprint. Discussion started: 31 January 2025

Using a similar technique, the downward brightness temperature in the dry firn region can be obtained by multiplying the term. $\exp\left(-\sec\theta\int_{-d}^{z'}\overleftarrow{\kappa_e}(\theta,z'')dz''\right)$ and integrate z' from $z'=z$ to $z'=0$. After some math, the downward brightness temperature can be simplified into the following:

$$\overleftarrow{T_d}(\theta,z)=\overleftarrow{T_d}(\theta,0)\exp\left(-\sec\theta\int_z^0\overleftarrow{\kappa_e}(\theta,z'')dz''\right)$$
$$+\sec\theta\int_z^0\kappa_a(z')T_0(z')\exp\left(-\sec\theta\int_z^{z'}\overleftarrow{\kappa_e}(\theta,z'')dz''\right)dz'$$
$$+\overleftarrow{W}(\theta,z)$$

Where:

$W(\theta,z)=$

$$\sec\theta\int_z^0 dz'\exp\left(-\sec\theta\int_z^{z'}\overleftarrow{\kappa_e}(\theta,z'')dz''\right)\int_0^{\frac{\pi}{2}}d\theta'\sin\theta'\left[\vec{P}(\pi-\theta,\theta')\vec{T}_u(\theta',z)+\vec{P}(\pi-\theta,\pi-\theta')\vec{T}_d(\theta',z)\right]$$

account for the scattering contribution to the downward directions.

Looking at the expressions for upward and downward going brightness temperatures, the boundary values on the right-hand side of the equations, $\vec{T}_u(\theta,z=-d)$ and $\vec{T}_d(\theta,z=0)$, are still unknown. Since the targeted unknowns in the radiative transfer equations are $\vec{T}_u(\theta,z)$ and $\vec{T}_d(\theta,z)$, The boundary values need to be canceled using the boundary condition equations.

By setting $z=0$ in T_u and $z=-d$ at $z=-d$, and use the boundary conditions to cancel out the terms $T_u(\theta,z=0)$ and $T_d(\theta,z=-d)$. The terms can be specified as:

$$\overleftarrow{T_u}(\theta,-d)=\left[I-\overleftarrow{r_{10}}(\theta)\vec{r}_{12}(\theta)\exp\left(-2\sec\theta\int_{-d}^0\overleftarrow{\kappa_e}(\theta,z'')dz''\right)\right]^{-1}$$
$$\left\{(1-\vec{r}_{12}(\theta))T_2+\vec{r}_{12}(\theta)\sec\theta\int_{-d}^0\kappa_a(z')T_0(z')\exp\left(-\sec\theta\int_{-d}^{z'}\overleftarrow{\kappa_e}(\theta,z'')dz''\right)dz'\right.$$
$$+\overleftarrow{r_{10}}(\theta)\vec{r}_{12}(\theta)\sec\theta\exp\left(-\sec\theta\int_{-d}^0\overleftarrow{\kappa_e}(\theta,z'')dz''\right)\int_{-d}^0\kappa_a(z')T_0(z')\exp\left(-\sec\theta\int_{z'}^0\overleftarrow{\kappa_e}(\theta,z'')dz''\right)dz'$$
$$+\overleftarrow{r_{10}}(\theta)\vec{r}_{12}(\theta)\exp\left(-\sec\theta\int_{-d}^0\overleftarrow{\kappa_e}(\theta,z'')dz''\right)\vec{S}(\theta,0)$$
$$\left.+\vec{r}_{12}(\theta)\overleftarrow{W}(\theta,-d)\right\}$$

$$\overleftarrow{T_d}(\theta,0)=\left[I-\vec{r}_{12}(\theta)\vec{r}_{10}(\theta)\exp\left(-2\sec\theta\int_{-d}^0\overleftarrow{\kappa_e}(\theta,z'')dz''\right)\right]^{-1}$$
$$\left\{\vec{r}_{10}(\theta)(1-\vec{r}_{12}(\theta))T_2\exp\left(-\sec\theta\int_{-d}^0\overleftarrow{\kappa_e}(\theta,z'')dz''\right)\right.$$

https://doi.org/10.5194/egusphere-2024-2395
Preprint. Discussion started: 31 January 2025

$$+\overleftrightarrow{r}_{10}(\theta)\sec\theta\int_{-d}^{0}\kappa_a(z')T_0(z')\exp\left(-\sec\theta\int_{z'}^{0}\overleftrightarrow{\kappa_e}(\theta,z'')dz''\right)dz'$$

$$+\sec\theta\overleftrightarrow{r}_{12}(\theta)\overleftrightarrow{r}_{10}(\theta)\exp\left(-\sec\theta\int_{-d}^{0}\overleftrightarrow{\kappa_e}(\theta,z'')dz''\right)\int_{-d}^{0}\kappa_a(z')T_0(z')\exp\left(-\sec\theta\int_{-d}^{z'}\overleftrightarrow{\kappa_e}(\theta,z'')dz''\right)dz'$$

$$+\overleftrightarrow{r}_{10}(\theta)\vec{S}(\theta,0)$$

$$+\overleftrightarrow{r}_{12}((\theta)\overleftrightarrow{r}_{10}(\theta)\exp\left(-\sec\theta\int_{-d}^{0}\overleftrightarrow{\kappa_e}(\theta,z'')dz''\right)\vec{W}(\theta,-d)\Big\}$$

Substitute back to the upward and downward expressions, and the brightness temperature expressions in Section II are obtained.

Validations of the Iterative Approach for Homogenous Dry Firn

In this case, the dry firn layer has a uniform mean density profile so that the iterative approach can be compared to the eigenvalue approach [Tsang et al. 2001]. The physical temperatures and density properties are all constant. The physical temperatures of the aquifer and dry fin are set as 273.15K and 265K, respectively. Assuming the aquifer has a liquid water content of 20%, through the full wave simulation approach, the corresponding permittivity value is 7.6+0.25i [Huang et al. 2024]. The mean density profile of the dry firn is set as 1.55g/cm^3, corresponding to a permittivity of 1.65 for the real part. For the imaginary part, the value of 0.01 is chosen to accelerate the convergence of the simulation. The density variation is characterized by a standard deviation of 0.05g/cm^3 with a vertical and horizontal correlation length of 5cm and 50cm, respectively. For both methods, 64 quadrature angles are selected to solve the same emission problem. In the iterative approach, contributions from each order are recorded to check the convergence of the solution. In Figure A1, up to the 9th order iteration, results are plotted for the V and H brightness temperature at 40 degrees as an example to illustrate the convergence. Brightness temperature as a function of observation angles is plotted in Figure A2 to compare the solutions.

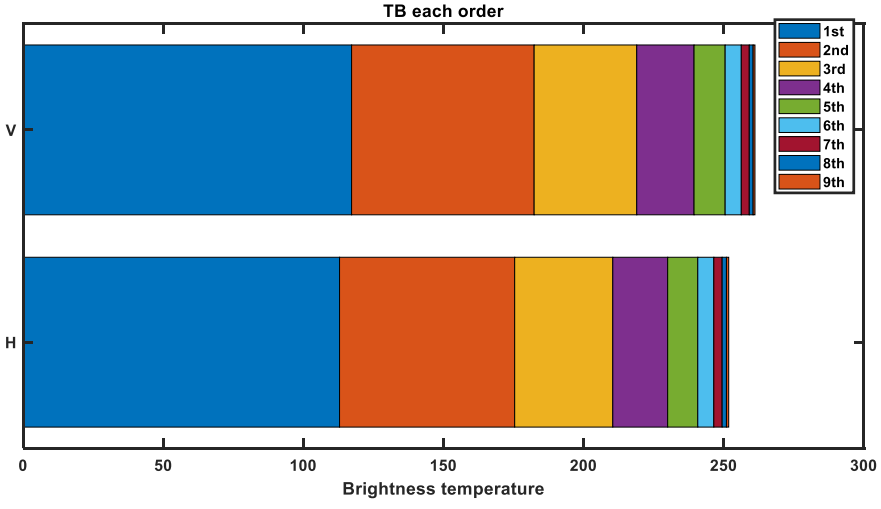

https://doi.org/10.5194/egusphere-2024-2395
Preprint. Discussion started: 31 January 2025

Figure A1 Contribution of brightness temperature from each order for 40 degrees. The first several orders are shown for this simple case. In this particular case, contributions beyond 2nd order have little contribution.

For this problem, the iteration approach calculates up to 30 orders. As indicated in Figure A1, the first five orders are the major contributors to the solution. Contributions from the 8th and 9th orders are much less significant. Only 1.3K and 0.65K are provided for these two orders in V pol 0.8K and 1.5K for H pol. The contributions from the iterations will be much lower as the order goes up. Brightness temperature predictions as a function of observation angles are provided in Figure A2. As it is shown, for both V and H polarizations, the two methods show good agreement with each other. The V polarization results first increase as the observation is close to the Brewster angle and then go down. At the same time, the H pol decreases monotonically.

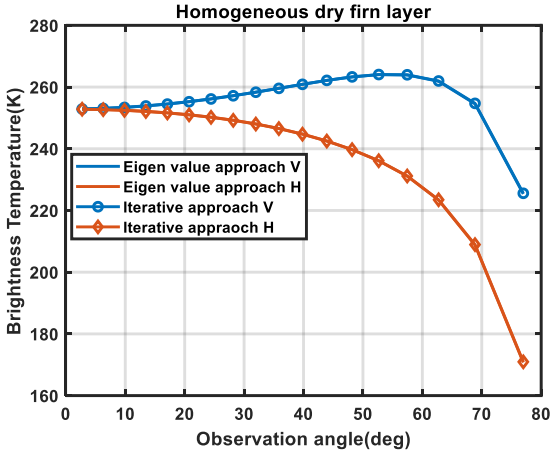

Figure A2 A single homogenous dry firn layer results from eigenvalue method and iterative approach. The results from the two methods agree very well with each other.

https://doi.org/10.5194/egusphere-2024-2395
Preprint. Discussion started: 31 January 2025

Appendix B. Accumulation Radar echogram near FA-13

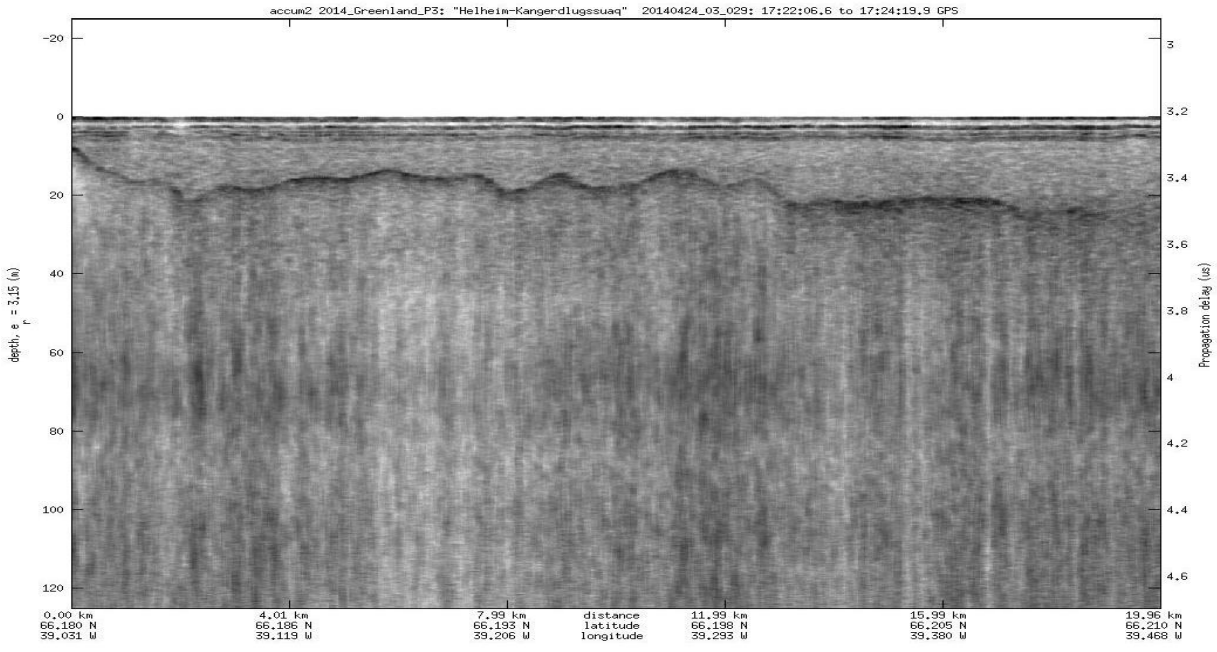

Figure B1 Accumulation Radar data in 2014 near FA-13

The accumulation radar echogram is provided in Figure B1, where the second location of (66.19N, 39.1865W) is in the middle left of the figure. According to the image, the area near the second location has a water table depth of around 15-16m. An average of 15.5m of water table depth is used for the simulation.

References

Baker, Ian. "Microstructural characterization of snow, firn and ice." Philosophical Transactions of the Royal Society A 377, no. 2146 (2019): 20180162.

Bamber, J.L., R. M. Westaway, B. Marzeion, B. Wouters, The land ice contribution to sea level during the satellite era. Environ. Res. Lett. 13, 63008 (2018).

Brangers, I., Lievens, H., Miège, C., Demuzere, M., Brucker, L., and De Lannoy, G. J. M.: Sentinel-1 detects firn aquifers in the Greenland ice sheet, Geophys. Res. Lett., 47, e2019GL085192, https://doi.org/10.1029/2019GL085192, 2020.

Bringer, A., Miller, J., Johnson, J. T., and Jezek, K. C.: Radiative transfer modeling of the brightness temperature signatures of firn aquifers, American Geophysical Union Fall Meeting, New Orleans, LA, U.S.A., https://agu.confex.com/agu/fm17/meetingapp.cgi/Paper/283159, 11–15 December 2017.

Chu, W., Schroeder, D. M., & Siegfried, M. R. (2018). Retrieval of englacial firn aquifer thickness from ice-penetrating radar sounding in southeastern Greenland. Geophysical Research Letters, 45, 11,770–11,778. https://doi.org/10.1029/2018GL079751

CReSIS, L1B accumulation radar product, ftp://data.cresis.ku.edu/data/accum/,2024

https://doi.org/10.5194/egusphere-2024-2395
Preprint. Discussion started: 31 January 2025

Dangendorf, S. et al. Persistent acceleration in global sea-level rise since the 1960s. Nat. Clim. Change 9, 705–710 (2019).

Ding, K.H., X. Xu, and L. Tsang, "Electromagnetic Scattering by Bicontinuous Random Microstructures with Discrete Permittivities," IEEE Trans. Geosci. Remote Sens., 48(8), 3139-3151, August 2010.

Entekhabi, D., et al., "The soil moisture active passive (SMAP) mission," Proc. IEEE, vol. 98, no. 5, pp. 704–716, May 2010.

Frederikse, T., Landerer, F., Caron, L. et al. The causes of sea-level rise since 1900. Nature 584, 393–397 (2020). https://doi.org/10.1038/s41586-020-2591-3

Forster, R., Box, J., van den Broeke, M. et al. Extensive liquid meltwater storage in firn within the Greenland ice sheet. Nature Geosci 7, 95–98 (2014). https://doi.org/10.1038/ngeo2043

Gregory, J. M. et al. Twentieth-century global-mean sea level rise: is the whole greater than the sum of the parts? J. Clim. 26, 4476–4499 (2013).

Koenig, L. S., Miège, C., Forster, R. R., and Brucker, L. (2014), Initial in situ measurements of perennial meltwater storage in the Greenland firn aquifer, Geophys. Res. Lett., 41, 81–85, doi:10.1002/2013GL058083

Long, D. G., M. Brodzik, and M. Hardman, "Enhanced resolution SMAP brightness temperature image products," IEEE Trans. Geosci. Remote Sens., vol. 57, no. 7, pp. 4151–4163, Jul. 2019.

Long, David Fawwaz Ulaby et al., *Microwave Radar and Radiometric Remote Sensing*, Artech, 2015.

Matzler, C.: Microwave permittivity of dry snow, IEEE T. Geosci. Remote, 34, 573–581, https://doi.org/10.1109/36.485133, 1996.

Miller, O., Solomon, D. K., Miège, C., Koenig, L., Forster, R., Schmerr, N., et al. (2020). Hydrology of a perennial firn aquifer in southeast Greenland: An overview driven by field data. Water Resources Research, 56, e2019WR026348. https://doi.org/10.1029/2019WR026348

Miller OL, Solomon DK, Miège C, Koenig LS, Forster RR, Montgomery LN, Schmerr N, Ligtenberg SRM, Legchenko A and Brucker L (2017) Hydraulic Conductivity of a Firn Aquifer in Southeast Greenland. Front. Earth Sci. 5:38. doi: 10.3389/feart.2017.00038

Miller, O., Solomon, D. K., Miège, C., Koenig, L., Forster, R., Schmerr, N., … Montgomery, L. (2018). Direct evidence of meltwater flow within a firn aquifer in southeast Greenland. Geophysical Research Letters, 45, 207–215. https://doi.org/10.1002/2017GL075707

Miège, C., Forster, R. R., Brucker, L., Koenig, L. S., Solomon, D. K., Paden, J. D., et al. (2016). Spatial extent and temporal variability of Greenland firn aquifers detected by ground and airborne radars. Journal of Geophysical Research: Earth Surface, 121, 2381–2398. https://doi.org/10.1002/2016JF003869

Miège, Clément, Richard Forster, Ludovic Brucker, Lora Koenig, Olivia Miller, Kip Solomon, and Nick Schmerr Firn temperatures (2013-2017) and water-level changes (2015-2017) collected at three locations in a firn-aquifer region of the southeastern part of the Greenland Ice Sheet https://arcticdata.io/catalog/view/doi:10.18739/A2R785P5W

Miège, C., Forster, R., Koenig, L., Miller, J., Miller, O., Montgomery, L., et al. (2020) "Density, hydrology and geophysical measurements from the Wilkins Ice Shelf firn aquifer" U.S. Antarctic Program (USAP) Data Center. Doi: https://doi.org/10.15784/601390.

Miller, J. Z., et al., "Brief communication: Mapping Greenland's perennial firn aquifers using enhanced-resolution L-band brightness temperature image time series," Cryosphere, vol. 14, no. 9, pp. 2809–2817, 2020.

Miller, J. Z. R. Culberg, D. G. Long, and C. A. Christopher, D. M. Schroeder, and M. J. Brodzik, "An empirical algorithm to map perennial firn aquifers and ice slabs within the Greenland ice sheet using satellite L-band microwave radiometry," Cryosphere, vol. 16, no. 1, pp. 103–125, 2022.

https://doi.org/10.5194/egusphere-2024-2395
Preprint. Discussion started: 31 January 2025

Montgomery, L., Miège, C., Miller, J., Scambos, T. A., Wallin, B., Miller, O., et al. (2020). Hydrologic properties of a highly permeable firn aquifer in the Wilkins Ice Shelf, Antarctica. Geophysical Research Letters, 47, e2020GL089552. https://doi.org/ 10.1029/2020GL08955

Montgomery, L., Koenig, L., and Alexander, P.: The SUMup dataset: compiled measurements of surface mass balance components over ice sheets and sea ice with analysis over Greenland, Earth Syst. Sci. Data, 10, 1959–1985, https://doi.org/10.5194/essd-10-1959-2018, 2018.

Nghiem, S. V., Hall, D. K., Mote, T. L., Tedesco, M., Albert, M. R., Keegan, K., Shuman, C. A., DiGirolamo, N. E., and Neumann, G. (2012), The extreme melt across the Greenland ice sheet in 2012, Geophys. Res. Lett., 39, L20502, doi:10.1029/2012GL053611.

Oppenheimer, M. et al. in IPCC Special Report on the Ocean and Cryosphere in a Changing Climate (eds Pörtner, H.-O. et al.) Ch.4 (2019).

Shepherd, A., Gilbert, L., Muir, A. S., Konrad, H., McMillan, M., Slater, T., ... & Engdahl, M. E. (2019). Trends in Antarctic Ice Sheet elevation and mass. Geophysical Research Letters, 46(14), 8174-8183.

Shepherd, A. , E. R. Ivins, G. A, V. R. Barletta, M. J. Bentley, S. Bettadpur, K. H. Briggs, D. H. Bromwich, R. Forsberg, N. Galin, M. Horwath, S. Jacobs, I. Joughin, M. A. King, J. T. M. Lenaerts, J. Li, S. R. M. Ligtenberg, A. Luckman, S. B. Luthcke, M. McMillan, R. Meister, G. Milne, J. Mouginot, A. Muir, J. P. Nicolas, J. Paden, A. J. Payne, H. Pritchard, E. Rignot, H. Rott, L. S. Sørensen, T. A. Scambos, B. Scheuchl, E. J. O. Schrama, B. Smith, A. V. Sundal, J. H. van Angelen, W. J. van de Berg, M. R. van den Broeke, D. G. Vaughan, I. Velicogna, J. Wahr, P. L. Whitehouse, D. J. Wingham, D. Yi, D. Young, H. J. Zwally, A reconciled estimate of ice-sheet mass balance. Science 338, 1183–1189 (2012).

Slater, T., Lawrence, I. R., Otosaka, I. N., Shepherd, A., Gourmelen, N., Jakob, L., Tepes, P., Gilbert, L., and Nienow, P.: Review article: Earth's ice imbalance, The Cryosphere, 15, 233–246, https://doi.org/10.5194/tc-15-233-2021, 2021.

Smith, B., Fricker, H. A., Gardner, A. S., Medley, B., Nilsson, J., Paolo, F. S., ... & Harbeck, K. (2020). Pervasive ice sheet mass loss reflects competing ocean and atmosphere processes. Science, 368(6496), 1239-1242.

Sihvola, A. H. Electromagnetic Mixing Formulas and Applications. IEE. (1999).

Stevens, M., Emmakahle, H. V., and Jboat: UWGlaciology/CommunityFirnModel: Version 1.1.6, Zenodo, https://doi.org/10.5281/ZENODO.5719748, zenodo, 2021.

Tiuri, M., Sihvola, A., Nyfors, E., and Hallikaiken, M.: The complex dielectric constant of snow at microwave frequencies, IEEE J. Oceanic Eng., 9, 377–382, https://doi.org/10.1109/JOE.1984.1145645, 1984

Tsang, L., Kong, J. A., and Ding, K. H.: Scattering of Electromagnetic Waves, 1: Theory and Applications, Wiley Interscience, 426 pp., ISBN 0-471-38799-7, 2000.

Xu, H., Medley, B., Tsang, L., Johnson, J. T., Jezek, K. C., Brogioni, M., and Kaleschke, L.: Polar firn properties in Greenland and Antarctica and related effects on microwave brightness temperatures, The Cryosphere, 17, 2793–2809, https://doi.org/10.5194/tc-17-2793-2023, 2023.

Xu, H., Electromagnetic modeling for the active and passive remote sensing of polar ice sheet and for Signal of Opportunity (SoOp) land observation, University of Michigan, Ph.D thesis

Data and code availability

The code is available upon request. All the data used in the paper is provided in the references.

https://doi.org/10.5194/egusphere-2024-2395
Preprint. Discussion started: 31 January 2025

Author contribution

Haokui Xu performs the major work. Leung Tsang and Brooke Medely provided suggestions on formulating the work and suggestions on the results. Julie Miller provided suggestions on the sensitivity analysis. Joel Johnson provided suggestions on the goal of the paper and the language.

Competing interests

The authors declare no competing interests.